JGR Planets

RESEARCH ARTICLE
10.1029/2022JE007290

Key Points:

- Low latitude tides compared at different altitudes show little interannual variation in dominant wavenumber with some seasonal variation
- Model-derived results compare better with observations at low altitude than at high altitude
- Estimates of energy suggest that most of the energy is dissipated below ~90 km

Correspondence to:

A. Kumar,
aishsk6@vt.edu

Citation:

Kumar, A., England, S. L., Liu, G., Jain, S., & Schneider, N. M. (2022). Observations of atmospheric tides in the middle and upper atmosphere of Mars from MAVEN and MRO. *Journal of Geophysical Research: Planets*, *127*, e2022JE007290. https://doi.org/10.1029/2022JE007290

Received 8 MAR 2022
Accepted 1 JUL 2022

Author Contributions:

Conceptualization: Aishwarya Kumar, Scott L. England
Data curation: Aishwarya Kumar, Scott L. England
Formal analysis: Aishwarya Kumar
Funding acquisition: Scott L. England
Investigation: Aishwarya Kumar
Methodology: Aishwarya Kumar, Scott L. England
Project Administration: Scott L. England
Resources: Scott L. England, Sonal Jain
Software: Aishwarya Kumar
Supervision: Scott L. England
Validation: Aishwarya Kumar, Scott L. England
Visualization: Aishwarya Kumar
Writing – original draft: Aishwarya Kumar

Observations of Atmospheric Tides in the Middle and Upper Atmosphere of Mars From MAVEN and MRO

Aishwarya Kumar[1], Scott L. England[1], Guiping Liu[2], Sonal Jain[3], and Nicholas M. Schneider[3]

[1]Aerospace and Ocean Engineering, Virginia Polytechnic Institute and State University, Blacksburg, VA, USA, [2]Space Sciences Laboratory, University of California Berkeley, Berkeley, CA, USA, [3]Laboratory for Atmospheric and Space Physics, University of Colorado Boulder, Boulder, CO, USA

Abstract Variability in the Martian upper atmosphere is strongly linked to the lower atmosphere and much of it can be attributed to vertical wave propagation. Atmospheric tides in particular are a well-known phenomenon in the Martian atmosphere that play a key role in the transport of energy as they propagate to higher altitudes. Previous theoretical predictions and observations suggest that tides producing wavenumber-2 and wavenumber-3 patterns are strongest in a fixed local time at high altitudes, however, the energy they carry and the region of deposition are not well characterized. Given the availability of atmospheric observations from several spacecraft at the same time, in this paper, the nature and behavior of tides are studied concurrently at several altitudes. Here, six intervals are identified focused at fixed low latitudes utilizing simultaneous observations of the middle and upper atmosphere from in situ and remote sensing instruments on different spacecraft. In the middle atmosphere, strong wavenumber-2 signatures are identified in the intervals north of the equator whereas, in the south, wavenumber-3 signatures are strongest. Wave signatures observed in the upper atmosphere seem to be dominated by a mix of wavenumbers-2 and -3. Seasonal variation is observed in the northern intervals, with very little interannual variability in all intervals considered. Estimates of energy based on dominant wavenumber amplitude suggest that most of the energy dissipates below ~90 km. Furthermore, model sampled output captures the dominant wavenumbers observed in the middle atmosphere as well as the energy dissipation characteristics.

Plain Language Summary Atmospheric tides are large-scale waves observed widely in the Martian atmosphere. Tides can carry energy and momentum as they propagate higher in altitude and deposit this energy in different regions of the atmosphere as they dissipate. While tides have been observed previously at different altitudes, it was not possible until recently to study them concurrently at different altitudes. Using observations from three instruments, here six cases at low latitudes and multiple altitudes are analyzed. At low altitudes to the north of the equator, a wave with two peaks in longitude is identified as strongest, but to the south, a wave with three peaks is strongest. The waves seen at high altitude are a mix of waves with two peaks and three peaks. The strongest wave observed changes with season in the north. For a particular season, there is very little year-to-year variability in the strongest wave observed. Comparing the estimated energy at different heights suggest that most of the energy is lost prior to ~90 km. Comparison of observations with model shows that the model is able to capture the strongest wave observed at lower altitudes. Moreover, this observed energy loss is also captured well by the model.

1. Introduction

Atmospheric tides are a significant feature in the Martian atmosphere owing to their very large scale and large amplitudes. Much of the longitudinal variability seen at thermospheric altitudes can be attributed to tides that propagate upward from the lower atmosphere. Furthermore, tides are capable of transporting energy and momentum from sources in the lower atmosphere to the upper atmosphere, thereby contributing notably to the energy and momentum budget of this region. Atmospheric thermal tides are seen as global scale oscillations in atmospheric fields such as density, pressure, temperature, and winds. The temporal period of these tides are fractions of the planetary rotation rate such as 24 hr (diurnal), 12 hr (semidiurnal) of local time, and so on.

Following the description in Forbes et al. (2002), tidal oscillations can be mathematically expressed as follows:

$$\sum_n \sum_s A_{n,s}(z,\theta).\cos\left(n\Omega t + s\lambda - \phi_{n,s}(z,\theta)\right) \quad (1)$$

Writing – review & editing: Aishwarya Kumar, Scott L. England, Guiping Liu, Sonal Jain, Nicholas M. Schneider

where Ω is the planetary rotation rate, t is the universal time in days, λ is the longitude with east positive, s is the zonal wavenumber and its absolute value is the number of cycles per 360° longitude, n is the temporal harmonic or the frequency. Components with $s > 0$ propagate westward and with $s < 0$ propagate eastward. If $n = 1$, the tide is diurnal and has a period of 1 day, if $n = 2$ the tide is semi-diurnal and has a period of half a day and, so on. $A_{n,s}$ and $\phi_{n,s}$ are the amplitude and phase that are functions of both altitude and latitude as can be seen in the above expression.

Equation 1 describes a tide in a fixed universal time (UT) frame, since spacecraft observations are often made in a fixed local time perspective, it is useful to describe the above expression in terms of local time where $t = t_{LT} - \frac{\lambda}{2\pi}$, therefore we get,

$$\sum_n \sum_s A_{n,s}(z,\theta).\cos\left(n\Omega t_{LT} + \lambda(s-n) - \phi_{n,s}(z,\theta)\right) \tag{2}$$

By referring to Equation 2, we see that there exist multiple combinations of n and s that can produce a non-migrating tide. For instance, a tide with wavenumber $|s - n| = 1$ where $n = 1$ and $s = 0$ has 1 cycle per 360° longitude in a fixed local time reference frame. For the same wavenumber 1, the values of n and s can also be $n = 2$ and $s = 1$; $n = 0$ and $s = 1$; $n = 1$ and $s = 2$ or $n = 2$ and $s = 3$. Satellite data generally helps in identifying $|s - n|$, but for a particular observed wavenumber, s and n can take on multiple values from which it can be only one of the combinations. Tides are commonly referred to in the literature by a combination of letters and numbers that describe their period, propagation direction and wavenumber (D, S stand for diurnal and semidiurnal respectively, W and E denote westward or eastward propagation, and $s = 1, 2, 3, 4$, etc. is the absolute zonal wavenumber). Therefore, DE1 stands for eastward propagating diurnal tide with zonal wavenumber 1.

Zurek (1976) highlighted the role of Martian surface topography in driving the diurnal tide through the modulation of thermal forcing comprised of heat flux from the surface or via absorption of solar radiation by a dusty atmosphere. It was noted that the topographic longitudinal wavenumber excites nonmigrating tidal components which can propagate vertically. In the past few decades, satellite-based observations have established the significance of non-migrating tides in the overall Martian tidal fields. Keating et al. (1998) showed that longitudinal variability in the inferred total mass density from MGS accelerometer measurements was characterized by wavenumber-2 at thermospheric altitudes and attributed this to the stationary planetary wave. Since many combinations of s and n could give rise to such an oscillation with $k = 2$, using the same data set for the same season and latitude as Keating et al. (1998) modeling results by Forbes and Hagan (2000) demonstrated that the DE1 tide can account for much of the wavenumber-2 variability.

Bougher et al. (2001), showed wavenumber-3 features associated with non-migrating tides in the electron density peak measurements and in the accelerometer measurements from MGS spacecraft observations. Large-scale longitudinal variations in densities derived from the MGS accelerometer data between 130 and 160 km were dominated by wavenumber-2 and wavenumber-3 features (Withers et al., 2003). Observations of the middle atmosphere between 70 and 120 km from the Mars Express SPICAM UV spectrometer were used to show zonal variations in pressure and temperature associated with non-migrating tides (Withers et al., 2011). This study also reported dominant wavenumber-2 and wavenumber-3.

Recent examinations of data from the Mars Atmosphere and Volatile Evolution (MAVEN) spacecraft have enabled the observation of tides in the upper atmosphere of Mars. Lo et al. (2015), showed the first observations of nonmigrating tides by inferring CO_2 densities from the CO_2^+UV—doublet emission measurements taken by the Imaging Ultraviolet Spectrograph (IUVS) on MAVEN. Strong wavenumber-2 and wavenumber-3 signatures from low to mid-latitudes were observed in a fixed local time frame, with wavenumber-2 having the largest amplitude (~29%) at the low latitudes. In a first combined analysis that used MAVEN remote sensing IUVS and in situ Neutral Gas and Ion Mass Spectrometer (NGIMS) observations, large-scale longitudinal structures were reported with a strong wavenumber-2 signature (England et al., 2016). This study also demonstrated the impact of vertical advection associated with nonmigrating tides on thermospheric composition. Liu et al. (2017) demonstrated similar longitudinal structures with underlying wavenumber-2 and wavenumber-3 patterns but with different amplitudes across two different seasons. Tidal signatures were also reported in the in situ neutral and electron density measurements, highlighting the coupling between I-T regions through atmospheric tides (Fang et al., 2021; Thaller et al., 2020). Schneider et al. (2020) identified the presence of wavenumber-3 structure in the NO nightglow brightness derived from MAVEN-IUVS in the middle atmosphere at low equatorial latitudes. On

further examining the phase of the wave with local time, the authors found that the predominant tide underlying the wavenumber-3 structure is the eastward moving diurnal tide with zonal wavenumber $s = 2$ (DE2). Strong wavenumber-3 structure was reported in the IUVS derived temperatures at 90 and 170 km during aphelion, while the wave amplitudes were significantly smaller during perihelion (Jain et al., 2021).

Owing to spacecraft geometry, most previous studies have only been able to determine $|s - n|$ wavenumbers since spacecraft tend to sample a wide range of longitudes over multiple orbits but these observations come from a set of similar local times. In order to establish the underlying tide present, the values of $|s|$ and $|n|$ need to be determined individually, which provides information about both the period as well as wavenumber of the tide. Lee et al. (2009) and Guzewich et al. (2012) have demonstrated the use of temperature retrievals from Mars Climate Sounder on Mars Reconnaissance Orbiter to extract tidal fields from a sun-synchronous orbit with equatorial crossing times at ∼3 a.m. and 3 p.m. LT. Such sampling allows for the separation of the semi-diurnal components from the diurnal components by examining differenced and averaged temperature fields computed from the two LTs that are ∼12 hr apart. Lee et al. (2009) was first to show that the diurnal tide dominated the tidal fields using Mars Climate Sounder (MCS) temperature retrievals. Guzewich et al. (2012) showed that the middle atmospheric amplitudes of wavenumber-2 were higher in the northern hemisphere between 10°–40°N and that it is clearly associated with the DE1 tide. Furthermore, it is also known that the eastward propagating tides are much more efficient in penetrating into the higher altitudes owing to their much longer vertical wavelengths and therefore such tidal modes are less impacted by molecular diffusion (Forbes et al., 2002, 2020).

Previously tides at Mars were observed at different altitudes but connecting these observations has been difficult due to a lack of data. Combination of observations from various instruments is now possible due to the availability of data over a broad range of altitudes, latitudes, local times and longitudes. The remote sensing IUVS and in situ NGIMS instruments aboard the MAVEN mission together provide density and temperature profiles between 120 and 200 km (Evans et al., 2015; Liu et al., 2017), whereas the remote sensing MCS instrument aboard Mars Reconnaissance Orbiter (MRO) provides temperature profiles between 30 and 90 km. This gives us the ability to observe the upper atmosphere (above ∼100 km) and middle atmosphere via remote and in situ measurements concurrently. Most recently, England et al. (2019) compared high latitude MAVEN IUVS and MAVEN NGIMS upper atmospheric data to MCS observations in the middle atmosphere. These observations suggest that the SE1 tide is most likely the cause of the observed wavenumber-3 signature in the southern hemisphere. Guzewich et al. (2012) examined the latitude-Ls structure using MCS temperature measurements at 76 km and compared it to the model output from Mars Climate Database at the same altitude. Good agreement was seen in the largest tidal component between observation and model results.

To investigate the impact of tides on the atmosphere as a whole, sampling is required across a broad range of altitudes. Following the approach described in England et al. (2019), in this study we combine the remote sensing and in situ data from MAVEN and MRO. This allows us to see how tides are evolving as they propagate vertically, and identify which ones reach the Martian upper atmosphere. Here, we examine the longitudinal structure and identify the underlying zonal wavenumbers above and below the Martian equator at low latitudes and at different altitudes. Taking advantage of the concurrent observations from MRO-MCS in the Martian middle atmosphere, we aim to identify which of the waves seen in the ∼30–80 km range make it to the Martian upper atmosphere, and how their amplitudes change between the altitudes sampled by MCS, IUVS and NGIMS, thereby providing information on their dissipation characteristics across this altitude range. In addition, the propagation direction, as well as an estimate of the period of the wave, is obtained using the MCS data. Given the dominant wavenumber and an estimate of the temporal period, to what degree are the tidal components capable of penetrating into higher altitudes? What is the non-migrating tidal spectrum sampled at the NGIMS and IUVS altitude at 165 and 140 km respectively and how does it relate to below this altitude? Focusing on two narrow latitude ranges, the variations in the tidal spectrum between different Martian seasons are studied. By utilizing the availability of the MCS data, repeatability of these tidal structures is also examined. Furthermore, the variations in density and temperature observed by MAVEN and MRO are also compared to the model-derived data from Mars Climate Database (MCD) allowing to assess the model's ability to capture tidal features at the sampled altitudes.

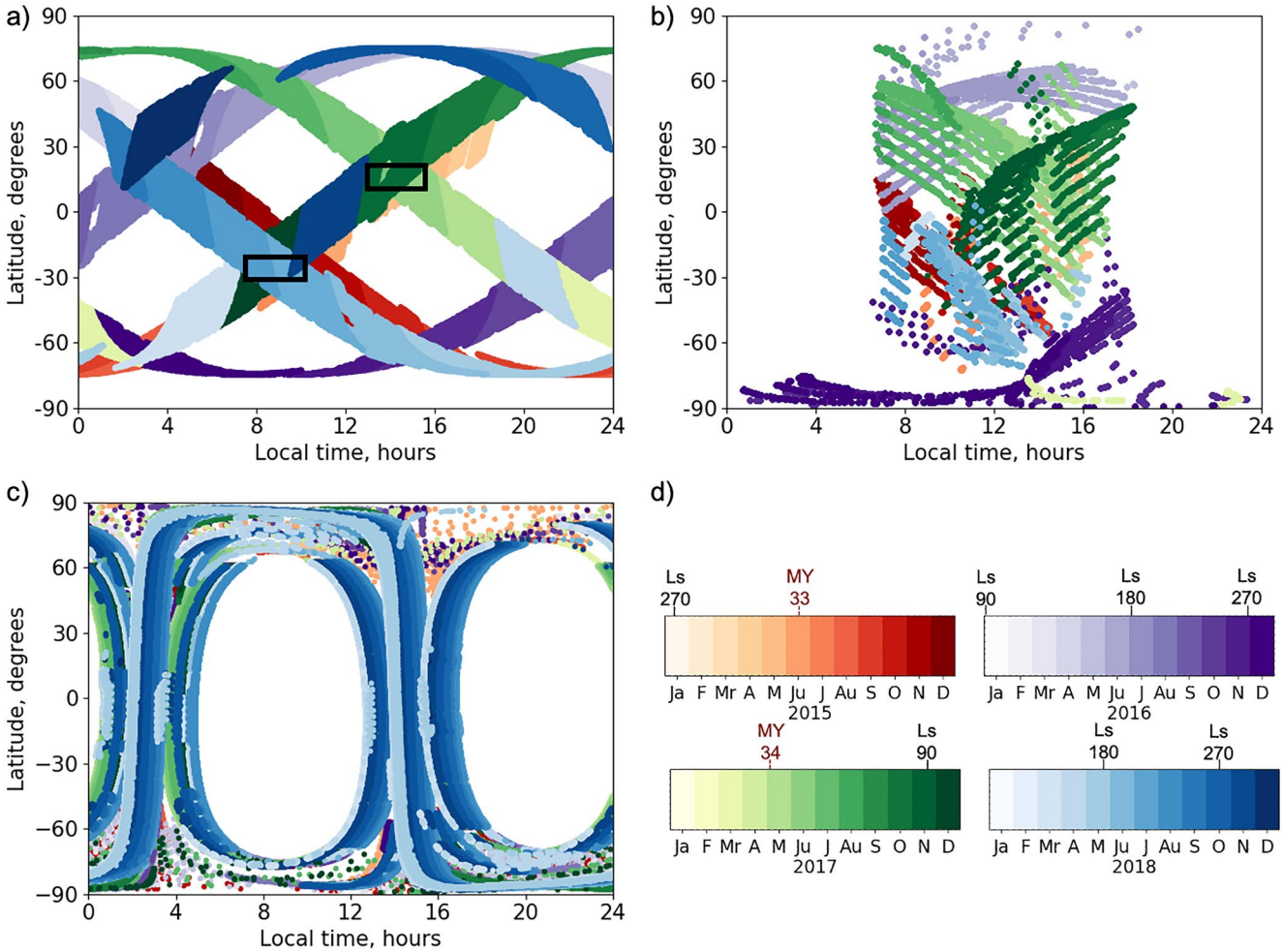

Figure 1. Distribution of the (a) NGIMS, (b) IUVS, and (c) MCS data used in this study. Black boxes in panel (a) shows the fixed latitude and local time ranges used to select the intervals to the north and south of the equator. Data are color-coded by month, ranging from January 2015 to December 2018. Several regions of overlap in the latitude-local time sampling can be seen, allowing seasonal changes to be identified at a single location.

2. Data Selection

This study utilizes observations derived from in situ measurements made with the Neutral Gas and Ion Mass Spectrometer (MAVEN-NGIMS) and remote sensing measurements made with the Imaging Ultraviolet Spectrograph (MAVEN-IUVS) and Mars Climate Sounder (MRO-MCS). In addition, we include data from the LMD-GCM's Mars Climate Database from here on referred to as MCD. While the analysis of tides ideally requires complete coverage in both longitude and time, multiple factors including spacecraft orbit, mission specific observational goals, instrument type etc., provide full coverage in either longitude or time, but rarely as a function of both parameters. To identify tidal signatures, and estimate the wavenumbers, propagation direction and period of the wave being observed, complete longitudinal coverage is required over a narrow range of latitudes. As seen in Equation 1, the amplitude of a tide is a strong function of latitude, therefore the selection of a large latitude range would result in mixing of the signal from wave amplitudes of different tides. The analysis here requires data sampled at different altitudes for a particular chosen latitude range. As tides are periodic in local time, dominant wavenumber can be examined by sampling tides at any local time. Therefore, we do not require perfect overlap in local time across multiple instruments but phase differences are expected as seen in Equation 2.

Figure 1a shows the complete NGIMS data coverage as a function of latitude and local time from February 2015 to December 2018 restricted in altitude range between 140 and 200 km. Data is chosen by defining a latitude-Ls box in a fixed local time range that is, (a) at low latitudes above and below the equator, (b) has repeated sampling over several time periods during the MAVEN mission, and (c) has both IUVS and NGIMS data. MCS data is

Table 1
The Six Cases Selected Based on NGIMS Data Coverage

NH cases	Mars year	Time period	Ls (°)	Season
Case A	32	5 March 2015–3 April 2015	[302–319]	Winter
Case B	33	1 April 2017–4 May 2017	[342–359]	Winter
Case C	34	22 September 2017–24 October 2017	[64–78]	Aphelion
SH cases	Mars year	Time period	Ls (°)	Season
Case A	33	30 October 2015–3 December 2015	[61–76]	Aphelion
Case B	34	25 November 2017–30 December 2017	[92–108]	Winter
Case C	34	19 May 2018–20 June 2018	[178–196]	Vernal equinox

Note. In the NH, the selected range lies within 15–25°N and 14–16.5 hr LT for case A, and 13.5–16 hr LT for the other two cases, and in the SH cases are within 15–25° S and 8–11 hr of local time.

almost always available at the same latitude as NGIMS observations. This also means that only IUVS data when the limb was sunlit will be used for this analysis. Thus, we end up with two regions: one north of the equator and the other south of the equator as shown in Table 1, each of which is sampled at three different time intervals corresponding to different Mars seasons and these are hereby referred to as cases (Cases A, B, and C respectively).

In order to extract tidal characteristics, complete longitudinal coverage is required for which many orbits of data need to be averaged. We use observations taken over a period of roughly a month in our analysis and we assume that tidal signatures will remain effectively constant over this time period. It is known that there is a lot of sol-to-sol variability but it is smaller than the longitudinal variability. MGS derived densities were used to show that longitudinal variability can be responsible for the densities to vary by a factor of two which was greater than the determined sol-to-sol variability (Withers et al., 2003). The timescales over which tidal signatures evolve in the Martian atmosphere range from several weeks to months, so it is fairly reasonable to utilize a month of data in the analysis which effectively removes the sol-to-sol variability as well (Mazarico et al., 2008; Withers et al., 2003).

2.1. NGIMS Data

NGIMS is a quadrupole mass spectrometer on MAVEN (Mahaffy et al., 2015) designed to make in situ composition measurements of neutral gas and ion species during the periapsis segment of the orbit below ∼500 km. The instrument alternates between two modes, a closed source mode: which measures non-reactive neutral species (e.g., CO_2, Ar, N_2, He), and an open source mode: which measures surface reactive neutral species (e.g., O, CO, and N) and ambient ions.

This study uses NGIMS level 2 (version 7, revision 3) data, and are publicly available on the Planetary Data System (PDS) at http://pds.nasa.gov (Benna & Lyness, 2014). In this data set, the raw detector counts are converted into derived densities for each species. To eliminate the impact of any interaction of CO_2 with the walls of the instrument after periapsis occurs in each orbit, we limit all NGIMS data to the inbound portion of each orbit (England et al., 2016). Owing to the ∼2.6 s cadence at which NGIMS measures the abundance of CO_2 alongside other species, there is a significant variation in the measured densities within just one periapsis segment of the orbit as well as between two consecutive orbits. This variation is associated with small-scale waves which are universally present in such in situ measurements. Hence, in order to clearly identify atmospheric tides above the strong signal of small-scale waves, any tidal analysis requires many orbits of NGIMS data (e.g., England et al., 2019; Liu et al., 2017).

The geometry of sampling for NH Case A during March–April 2015 is shown in Figures 2a–2c, Figure 2a shows the chosen data (inbound portion of orbit only) covers 15°–25°N latitude, and 14–16.5 hr of LT. The NGIMS data available for this time period offers complete longitudinal coverage over the given latitude range as shown in Figure 2b. There are gaps in the altitudinal coverage as seen in Figure 2c and therefore we limit our altitude range between 160 and 180 km where there is sufficient data at all latitudes. The data spans 2.5 hr of local time, and it

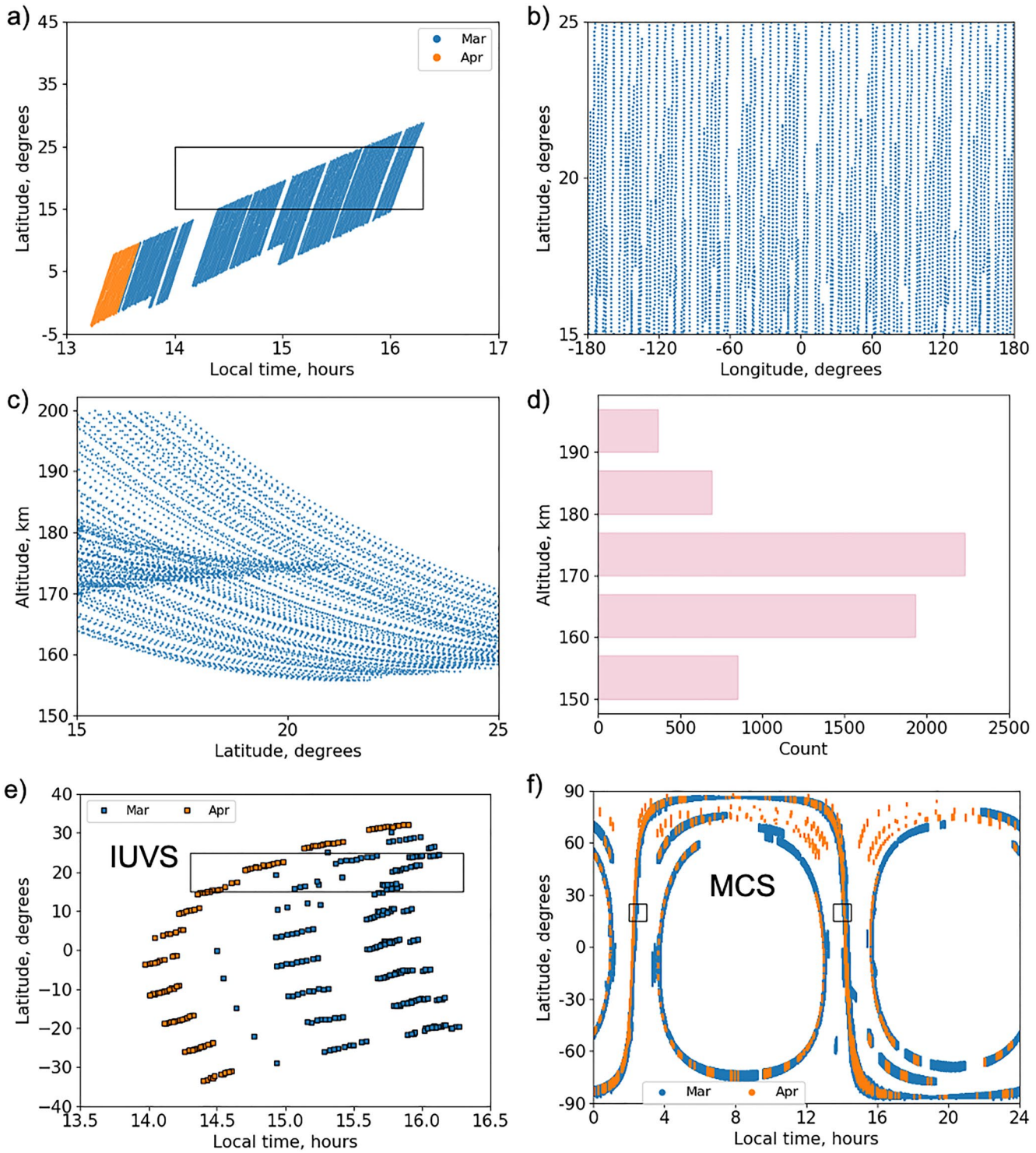

Figure 2. (a) NGIMS data for NH Case A (March–April 2015) shown as a function of latitude and local time. The black box denotes the latitude and local time range chosen for analysis (b) Location of NH Case A data as a function of latitude and longitude (c) Same as panel (b) but as a function of altitude and latitude for NH Case A and (d) Shows the number of data points in each altitude bin within the defined latitude range. (e) IUVS L2 data as a function of latitude and local time for the defined March–April 2015 period (NH Case A). The black box marks the range of data chosen for NH Case A analysis. (f) Mars Climate Sounder data where the dots indicate the location of the observations and the black box shows the latitude and local time ranges used in the study for NH Case A.

is assumed all the data come from a single local time. While this assumption might underestimate the apparent amplitude of the observed tides, they can still be identified since the local time range is small compared to the period of the diurnal and semidiurnal tides.

2.2. IUVS Data

IUVS is a remote sensing instrument on MAVEN that measures UV spectra of the atmospheric gas (McClintock et al., 2015). During the periapsis portion of the orbit, IUVS performs limb altitude scans when the spacecraft is below ∼500 km. The IUVS data used in this study are level 2, version 13 revision 1 and are publicly available on the Planetary Data System (PDS) at http://pds.nasa.gov (Deighan, 2015). This data set includes vertical profiles of CO_2 densities and temperatures derived from the periapsis limb observations during daytime (Evans et al., 2015). The CO_2^+UV-doublet dayglow emission is used to retrieve CO_2 density profiles and since there is no equivalent nightglow emission, the analysis is restricted to periapsis scans when the limb was sunlit with solar zenith angles (SZA < 75°).

Figure 1b shows the distribution of all available IUVS data from March 2015 to June 2018 and Figure 2e shows that the IUVS data are available in the same latitude region as the NGIMS observations for NH Case A. The IUVS level 2 data are on a fixed altitude grid and for the purposes of this study, data is sampled at 140 km which is roughly at the lower bound of the thermosphere. The selected data spans a local time range from 14.3 to 16.2 hr which represents a slightly different set of local times than the NGIMS data and is offset by ∼0.3 hr in local time. This discrepancy will only be reflected as a small phase difference in the tides identified in the two data sets since the expected tidal signatures are believed to have a period of 12–24 hr LT.

In addition to the IUVS level 2 data, we also have temperature data derived from the IUVS periapse level 1C (version 13, revision 1) data using the method described in Jain et al. (2021). This data set can be found in NASA's Planetary Data System (PDS) at https://atmos.nmsu.edu/data_and_services/atmospheres_data/MAVEN/maven_iuvs.html. As described in Jain et al. (2021), to extract temperatures in the middle atmosphere (∼90–105 km) from the IUVS observations, Chapman fits are performed on the O I 297.2 nm emission and the scale height is determined. The authors fit the measured intensity to the integral of the volume emission rates which is parametrized as a Chapman profile by using a Levenberg–Marquardt least squares minimization algorithm. Temperature variations can be therefore characterized by determining the value of the scale height using this Chapman approximation. All derived mesospheric temperatures derived from the L1C data are limited to periapse scans taken when solar zenith angle is below 85°. This new data set provides an excellent opportunity for comparison with the MRO-MCS data whose upper boundary is also near 90 km.

2.3. MCS Data

The MCS instrument on MRO is a limb and nadir scanning infrared radiometer that takes measurements of the surface and atmosphere of Mars (McCleese et al., 2007). MCS is a passive nine-channel radiometer out of which eight operate in the mid-infrared/far-infrared region and one in the broadband visible/near-infrared region. The temperature profiles are retrieved from the 15 μm CO_2 band between ∼30 and 90 km.

Using the same date range as that for NGIMS, data are available in the same latitude range for NH Case A. The data coverage for NH Case A is shown in Figure 2f. MRO is in a nearly polar sun-synchronous orbit such that the spacecraft's local solar time remains constant near 3 a.m. and 3 p.m. during the ascending and descending portions of the orbit. As seen in Figure 2f this changes as the spacecraft moves poleward of 75°N or S in latitude shifting from 3 p.m. to 3 a.m. and vice versa. Observations from this type of orbit provides good global coverage but at fixed local times as the planet rotates under the spacecraft.

2.4. Mars Climate Database

MCD is a database that provides atmospheric statistics derived from Global Climate Model (GCM) simulations (Forget et al., 1999; Millour et al., 2017). MCD provides mean values and statistics of meteorological variables like pressure, temperature, winds, atmospheric density, atmosphere composition and gases concentration, CO_2 ice surface layer, etc. These fields are averaged and stored 12 times a day on a 5.625° × 3.75° longitude-latitude grid, for 12 Martian months. Each Martian month spans 30° in solar longitude (Ls) which is roughly 50–70 Earth days.

The MCD consists of different scenarios based on the combination of dust and solar variability since these two forcings vary greatly from 1 year to another. Here we choose to use the "Mars Years" scenarios (MY24–MY33) which take into account the daily evolving solar EUV input and dust loading and therefore describes the Martian climate for each specific year to the best possible accuracy. While the analysis here consists of observations from MY32, MY33, and MY34, the current version of MCDv5.3 only extends its simulation results up to MY33. Assuming that the conditions do not vary much from year to year for a particular Ls range, we use MCD results from MY33 in place of MY34 for all cases that fall under MY34.

3. Analysis and Results

In this section, the method of analysis for each data set and the corresponding results will be discussed in the context of NH Case A only. The following subsections are ordered such that the method and results below 90 km, referred to as low altitude are discussed first followed by those above 130 km and are referred to as high altitude. Additionally, MCD model output is analyzed for each data set and compared at each altitude, both at low as well as high altitude.

3.1. MCS Results

As mentioned in Section 2.3, the MCS observations are almost always sampled near 3 a.m. and 3 p.m. local time which is roughly 12 hr apart in LT. We first constrain our latitudes between 15° and 25° N and choose a 1 hr local time window centered at ∼2.5 a.m. and 2 p.m. respectively. The temperature retrievals selected in each of these ranges are binned into 12 longitude bins (in 30° longitude steps) and 13 altitude bins (in 4 km altitude steps). Following England et al. (2019) we note that the diurnal components can be identified by subtracting the descending node data from the ascending node whereas the semidiurnal components as well as the zonal mean can be identified by summing these two together. A wavenumber 1–4 fit is performed at each altitude step and the fitted parameters are used to reconstruct wavenumber-2 and wavenumber-3 for each case. The uncertainties are computed by taking into consideration the geophysical variability or the spread in the data as noise rather than the stated noise from each instrument. The stated uncertainties are usually smaller than the variability in the atmosphere itself and are therefore not used to constrain the fit (Withers et al., 2003). For all cases to the north of the equator, MCS data extends up to 90 km, whereas in the south it extends only up to 82 km. In order to compare the wavenumbers between both the north and south within the MCS data itself, wave amplitudes are derived at 80 km altitude. In addition to this, since the low altitude IUVS data is derived at 90 km which also happens to be the upper bound of the MCS retrievals in the NH, to compare wavenumbers alone with the IUVS data at this altitude, the MCS wave amplitudes at 84 and 88 km are averaged. Given that there is no change in the dominant wavenumbers at the top five altitude bins, averaging the top two altitude bins allows for maximizing the signal, making the derived wave amplitudes robust. These values are not reported in the tables but the results are discussed when comparing dominant wavenumbers derived from both data sets in Sections 3.2 and 5.

Figure 3 shows clear wavenumber-2 and wavenumber-3 structures in the temperatures for NH Case A. But the scale of amplitude variation shows that wavenumber-2 dominates, followed by some wavenumber-3. The wavenumber-2 structure is visible in both the sum and difference panels, at altitudes above ∼50 km in the sum panel and above ∼70 km in the difference panel. On comparing the amplitudes of the signatures at 80 km, we see that wavenumber-2 in the differenced data has the largest amplitude, thereby making the diurnal component dominant over the semidiurnal. The phase of the wave here is defined as the longitude of the first peak east of longitude 0°. The vertical phase progression seems to move eastward with altitude between 60 and 80 km as seen in Figure 3 panel (c) suggesting that the underlying tide could be the DE1 tide. Withers et al. (2011) examined the phases of wavenumber-2 and wavenumber-3 components derived from pressure and temperature measurements taken by the Mars Express SPICAM UV spectrometer. It was found that the wavenumber-2 component is dominated by the DE1 tide above 80 km.

3.2. IUVS Results at 90 km

The low altitude IUVS derived temperatures were generated for the specific time periods of the cases discussed here. In order to have sufficient data coverage the date range is extended by 2 weeks but centered on the same date as for NH Case A. The chosen latitude range remains 15°–25°N and the LT range spans 14–16 hr which is offset by less than a half hour compared to the high altitude IUVS data.

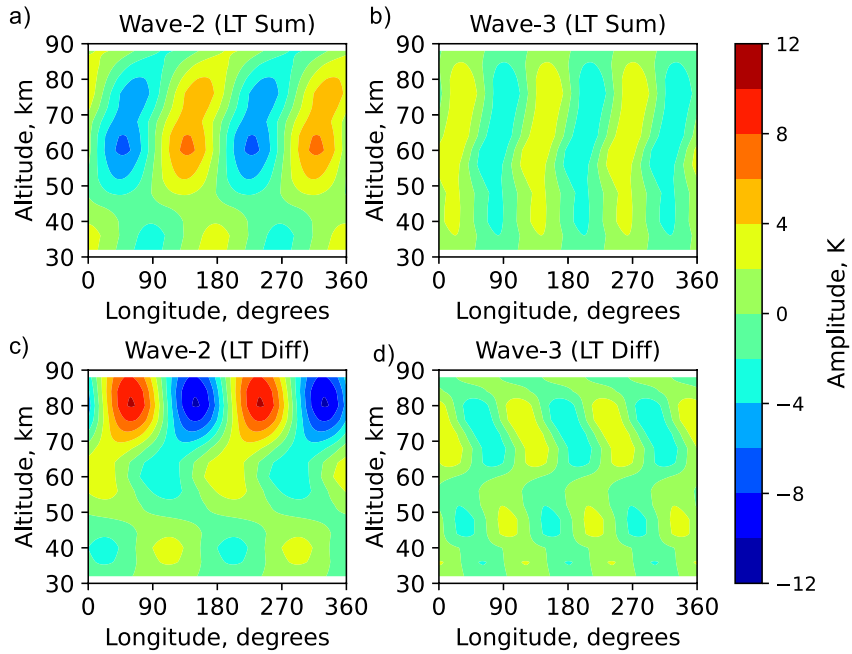

Figure 3. Reconstruction of the sum and difference of the wavenumber-2 and -3 fits to the MRO-MCS temperature data for NH Case A. Separate wavenumber 1–4 fits are performed at each 4-km altitude step on the temperature data around the ascending and descending nodes. Panels (a and b) show the temperature sum of the ascending and descending nodes, whereas panels (c and d) show the difference between these.

The derived temperatures as a function of longitude along with the wavenumber 1–4 least squares fit performed on the data is shown in Figure 4. Wavenumber-2 is identified as the dominant signature in the IUVS temperatures at 90 km and this is can be directly compared with the MCS results at 88 km shown in Figure 4b. The IUVS derived wave amplitudes are larger than those seen by MCS, which is likely due to the smaller number of IUVS data points available in this case. Small changes in amplitude and phase are usually averaged out if more data points are included, the lack thereof could result in larger amplitudes. It is worth noting that the MCS temperatures are binned and averaged in 30° by 4 km longitude-altitude bins as mentioned in Section 3.1, whereas the IUVS temperatures are not. The MCS temperatures are further broken down into its sum and difference components as seen in Figure 4 panels (c and d). It can clearly be seen that almost all of the wave can be attributed to the diurnal component shown in panel (d).

3.3. Comparison of MCD to Observations at Lower Altitudes

In this section, the longitudinal structure, wavenumbers and wave amplitudes at three altitudes-72, 80, and 88 km from the MCD are compared with MCS observations at the same altitudes. Since the data sets used in this analysis do not consist of a single observation type that spans the selected range, including model derived data provides a means to verify the internal consistency when compared with the high altitude observations. Forbes et al. (2020) compared seasonal-latitudinal structures and amplitudes from MCS observations at 76 km to MCD model output at 76 km and found reasonably good agreement. Given this result at lower altitude, it will also be useful to understand whether the MCD model output compares well with the high altitude observations.

Similar to the MCS observations, analysis of the MCD model output is carried out by the methodology described in Section 3.1 for the same latitudes and local time ranges selected for NH Case A. Wavenumber 1–4 fits to the LT summed and differenced model derived data are performed independently at each altitude as shown in Figure 5.

As seen in Figure 5, a clear wave structure can be seen at all three altitudes in both the sum and differenced panels of the model output and observations. The phase of the wave is consistent between the altitudes being compared in each panel as well as between model output and observations. The derived wave amplitudes at 80 km are shown in Table 2 alongside the wave amplitudes from MCS at 80 km and IUVS at 90 km.

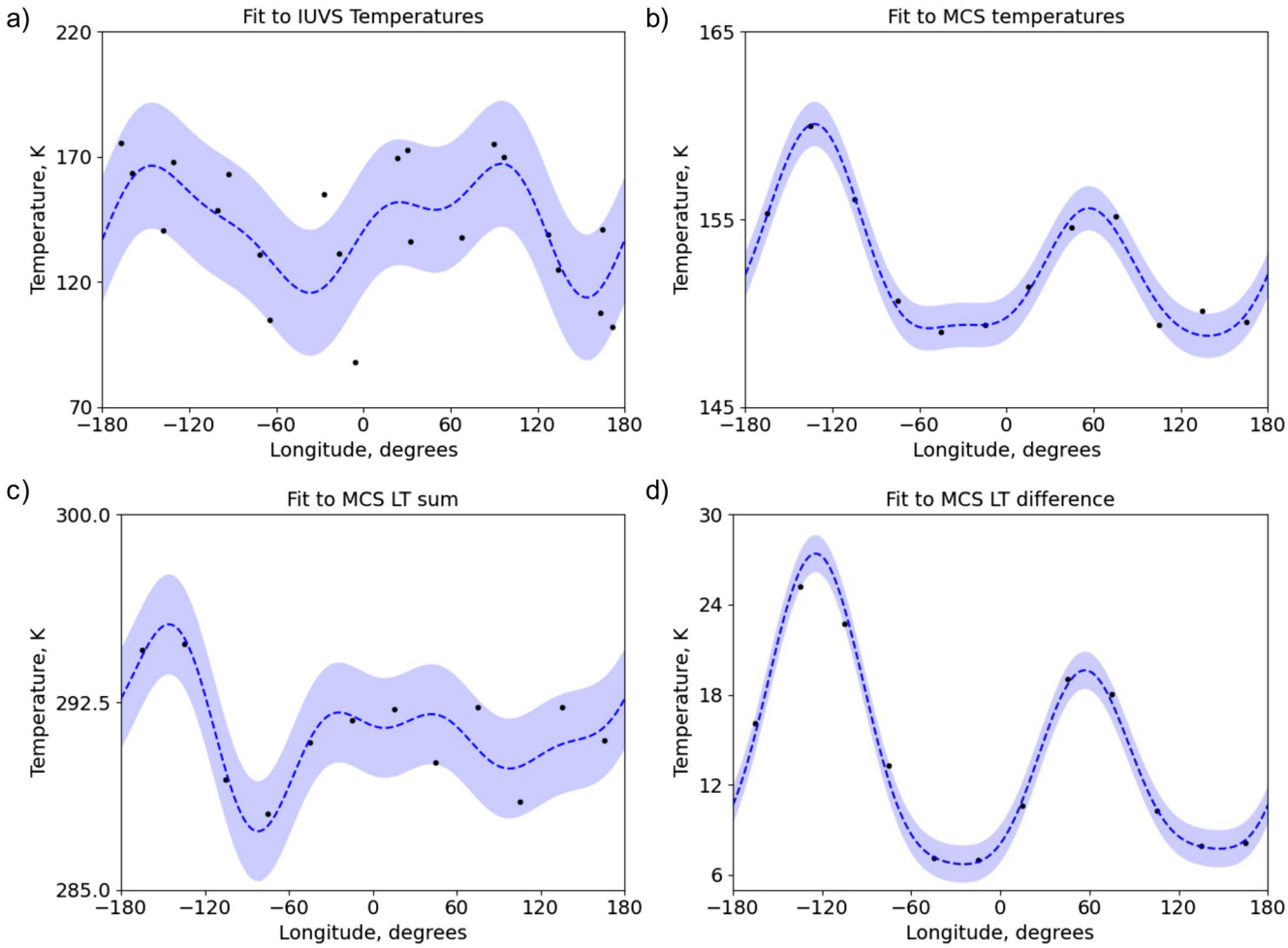

Figure 4. Panel (a) shows the temperatures derived from the O 297.2 nm dayglow emission at 90 km from IUVS observations over 15–25°N for Case A (1 March 2015–3 April 2015). The black dots show the raw derived temperatures as a function of longitude, the dashed blue line shows the reconstruction of the wavenumber 1–4 fit to the data and the shaded region shows the ±1 standard deviation from this fit. Panel (b) shows the binned and averaged Mars Climate Sounder (MCS) derived temperature sampled at 88 km and at the same location and local time as the IUVS data. Panels (c and d) show the LT sum and difference components of the MCS temperature data shown in panel (b).

It is clear that wavenumber-2 is the strongest component, which is in good agreement with both MCS and IUVS observations. In addition, the model output results also capture the diurnal component as dominant, which is again in reasonably good agreement with the MCS observations. It can also be seen that the mean temperatures agree well at this altitude.

3.4. IUVS Results at High Altitude

Perturbations in both CO_2 densities and temperatures are examined here using the IUVS level 2 data. Since IUVS level 2 density and temperature retrievals are on a fixed altitude grid, data from 140 km is used in this study. This ensures that we select data from just above the airglow peak and provides sufficient data for the analysis. From Figure 2e, we see that we have good overlap in latitude from 15° to 25°N covering the same range as NGIMS and MCS for NH Case A. The temperatures and densities at 140 km, within the selected latitude and local time range are shown in Figure 6 along with the wavenumber 1–4 least squares fit to the data.

In both panels (a and b) of Figure 6, a clear wavenumber-2 structure can be seen in both the density and temperature plots. There seems to be some asymmetry that suggests the presence of other wavenumbers which are

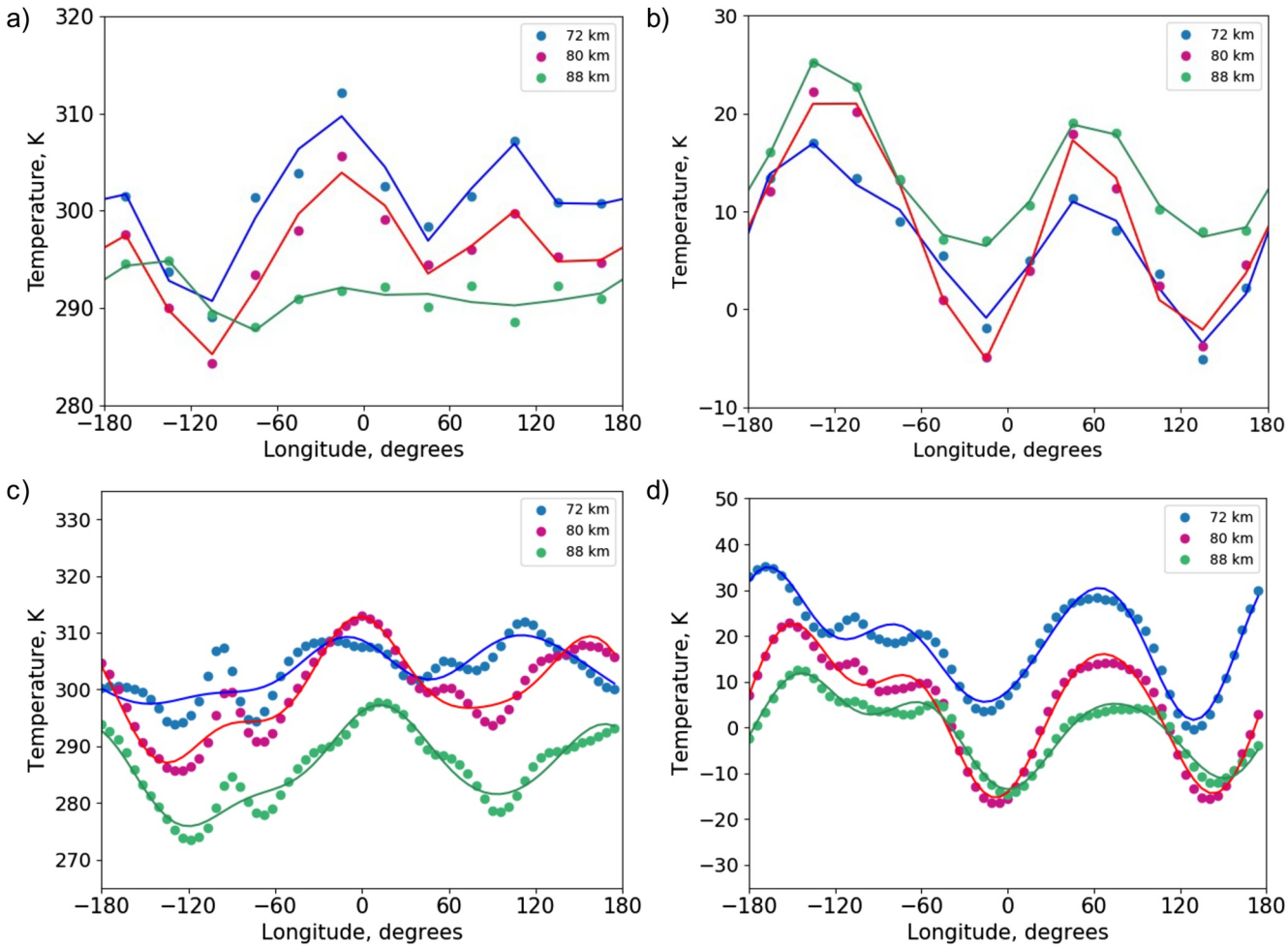

Figure 5. Comparison of the wavenumber 1–4 fit results of Mars Climate Database (MCD, bottom panels) and the Mars Climate Sounder (MCS) observations (top panels) at three altitudes. Panels (a and c) compare the reconstruction of LT summed data whereas panels (b and d) compare the LT difference reconstruction between MCS and MCD respectively.

captured in the fit as seen in Table 3. The signature in the temperature data is almost in anti-phase with the density variation which is also reported by England et al. (2019). The amplitudes listed in Table 3 show that wavenumber-2 dominates in both densities and temperatures with some wavenumber-3. These results are in good agreement with the NGIMS data at 165 km discussed in the following sub-section.

Table 2
Amplitudes of the Wavenumber 1–4 Fits to the MCS and IUVS Data at 80 and 90 km Respectively Compared to MCD for NH Case A

NH Case A Ls 310°	IUVS T (K) @ 90 km (20°–30°N)	MCD T (K) @ 90 km (20°–30° N)	MCS MY 32 T (K) @80 km		MCS MY 28–32 T (K) @80 km		MCD T (K) @80 km	
Mean	143 ± 5.5	139	147.86 ± 0.48		146.41 ± 1.73		150 ± 0.26	
			LT sum	LT diff	LT sum	LT diff	LT sum	LT diff
Wave 1	6.1 ± 6.7	0.3	1.9 ± 1.5	2.1 ± 1.7	1.1 ± 0.3	1.9 ± 0.7	2.76	2.81
Wave 2	**18.9 ± 7.6**	1.73	**2.1 ± 1.5**	**5.1 ± 1.5**	**2.3 ± 0.4**	**4.4 ± 0.6**	**3.87**	**6.38**
Wave 3	8.5 ± 6	**1.92**	1.6 ± 1.2	1.7 ± 1.4	0.7 ± 0.3	1.2 ± 0.8	1.48	3.95
Wave 4	8.6 ± 7.3	1.37	0.9 ± 1.5	0.1 ± 1.3	0.6 ± 0.2	0.9 ± 0.2	1.26	1.55

Note. The strongest wave amplitude in each column associated with data sets from each IUVS, MCS and MCD are boldfaced. Uncertainties are reported only for the observations.

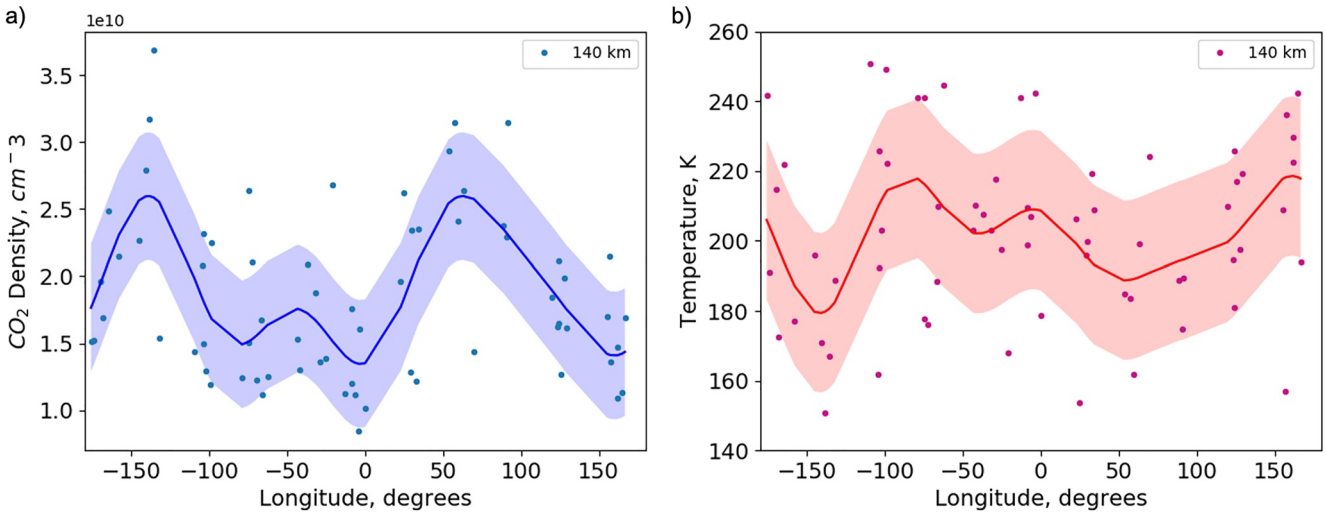

Figure 6. CO_2 density panel (a) and temperature panel (b) data from Imaging Ultraviolet Spectrograph (IUVS) observations at 140 km for the same latitude and LT ranges defined for NH Case A as shown in Figure 2e. The solid lines show the reconstruction of a wavenumber 1–4 fit to the data, and the shaded region shows the ±1 standard deviation from this fit. Densities are shown in blue; temperatures are shown in red.

3.5. NGIMS Results

The NGIMS data must be binned into regular altitude steps prior to any tidal analysis. In order to capture the variation with altitude in sufficient detail, 10 km altitude bins are chosen (Liu et al., 2017). However, since the individual NGIMS observations are at significantly higher altitude resolution, we calculate the mean value over 10 km altitude for a single orbit, in 1 km steps. The contour plots are then produced by computing the mean value at each altitude bin in 30° longitude bins.

A clear wave structure can be identified in Figure 7a which shows the mean observed CO_2 number density as a function of altitude and longitude. This wave structure appears at 160 km and continues to be visible up to ∼180 km although the densities near 180 km are relatively small.

Wave number fits similar to those shown for the IUVS observations in Section 3.4 are performed at the altitude bin with the highest number of data points in the NGIMS data. Based on the density of data points as shown in Figure 2d, for NH Case A the altitude chosen is 165 km and the corresponding orbit averaged CO_2 densities at this altitude are shown in Figure 7b. As with the corresponding IUVS data shown in Figures 6a and 6b and from Table 2, it is clear that the zonal wavenumber-2 component is dominant in the NGIMS observations at 165 km, but asymmetries in this suggest the presence of other wave numbers.

3.6. MCD Results at High Altitude

Forbes et al. (2020) examined MCD height-latitude structures of relative density perturbations which suggest vertical propagation of the DE1, DE2, and DE3 tidal components with expected density perturbations ranging from 15% to 25% in the 100–170 km altitude range. Further, this paper compares the MCD density perturbations to those derived from the Phase-II aerobraking of MGS between 105 – 115 km and find that MCD captures the dominant wavenumber-2 structure seen in MGS very well.

In this section, we extend our analysis to include a comparison of the MCD temperatures and density perturbations to those derived by the IUVS and NGIMS at high altitude (González-Galindo et al., 2015). MCD model output is sampled for the same latitude and local time ranges described for NH Case A. This model data is then analyzed in an identical manner wherein the temperatures and densities are binned and averaged as described in Sections 3.4 and 3.5 respectively.

The IUVS and NGIMS sampled MCD do not capture the dominant wavenumber-2 structure seen consistently throughout all high altitude observations. Instead, wavenumber-3 is strongest, followed closely by wavenumber-2 at both altitudes as seen in Figure 8. This is also in contrast with the low altitude where the MCS sampled MCD output captures the wavenumber-2 seen in MCS.

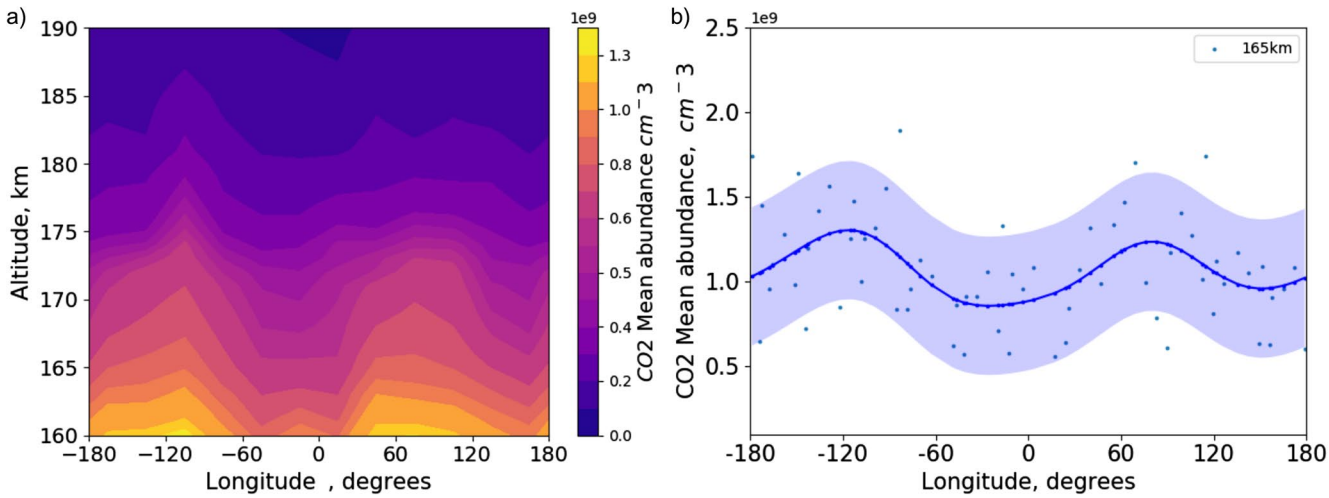

Figure 7. Longitudinal variations in the CO_2 number density as observed by NGIMS. (a) The mean number density observed between 15° and 25°N as a function of altitude and longitude (east positive). Mean values are shown in 10 km altitude bins (at 1 km steps) and 30° longitude bins. (b) The dots represent the 10 km vertical mean number densities for each of the orbits, the wavenumbers 1–4 fit to these data (blue solid line), and the range in this fit are based on the spread of the data (blue shaded region). The values shown are for the 10 km vertical bin centered at 165 km above the areoid.

3.7. Results for Cases North of the Equator

In this section, we will compare the results for all cases north of the equator, referred to as NH hereafter. The cases are ordered by date, March–April 2015: Case A (MY 32, Ls = 310°), April–May 2017: Case B (MY 33, Ls = 350°), both during northern winter and September–October 2017: Case C (MY34, Ls = 71°) during aphelion. The same analysis techniques described in previous sections are applied to each case. The results for each case are divided by altitude such that wavenumbers at low altitude, below 90 km from MCS and IUVS are summarized in Tables 2, 4, and 6 whereas high altitude IUVS and NGIMS are shown in Tables 3, 5, and 7. Having cases from three different Mars years also gives insight into interannual variability. To aid with understanding interannual variability, in addition to the three MY cases, MCS wave amplitudes at 80 km for the same Ls as the cases in question but for different Mars years from MY 28–32 are averaged and are shown to compare the 1 year result to the multi-year averaged result. Furthermore, the wavenumbers from the MCD model output compared to both low and high altitudes observations are also shown.

Table 3
Amplitudes of the Wavenumber 1–4 Fits to the IUVS and NGIMS Data at 140 and 165 km Compared to MCD for NH Case A

NH Case A Ls 310°	IUVS T (K) @ 140 km	MCD IUVS T (K) @140 km	IUVS ρ (%) @ 140 km	MCD IUVS ρ (%) @ 140 km	NGIMS CO_2 ρ(%) and Ar ρ(%) @ 165 km	MCD NGIMS ρ (%) @ 165 km
Mean	201.4 ± 3.1	171	1.91e10 ± 6.32e8	7.12e9	1.07e9 ± 3.83e7	7.12e8
					2.52e7 ± 8.81e5	
Wave 1	3.6 ± 4.5	1.2	9.2 ± 4.8	1.4	7.8 ± 5.1	1.9
					8.9 ± 4.9	
Wave 2	**9.9 ± 4.3**	2.0	**23.4 ± 4.7**	9.6	**16.2 ± 5.1**	10.3
					14.4 ± 4.9	
Wave 3	8.4 ± 4.4	**2.5**	13.4 ± 4.8	**11.4**	2.1 ± 5.0	**11.8**
					3.4 ± 4.9	
Wave 4	6.8 ± 4.6	0.9	10.0 ± 5.0	2.3	1.9 ± 5.0	2.1
					2.3 ± 4.9	

Note. The strongest wave amplitude in each column associated with data sets from each IUVS, NGIMS and MCD are boldfaced. Uncertainties are reported only for the observations.

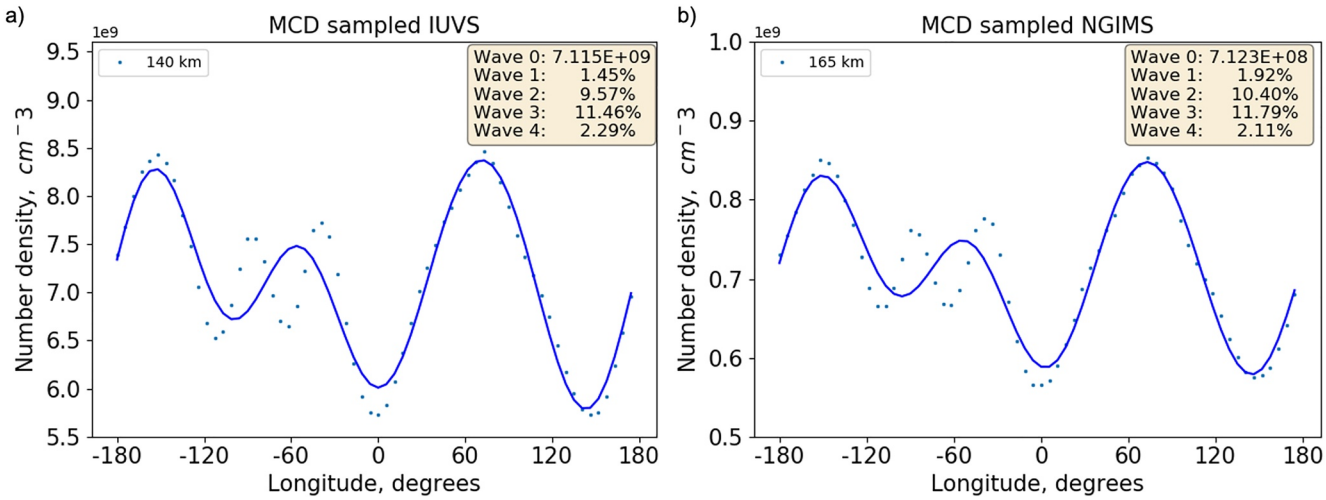

Figure 8. Mars Climate Database derived model output sampled at (a) IUVS and (b) NGIMS altitudes that is, at 140 and 165 km respectively. The blue dots represent the derived densities and the blue line is the wavenumber 1–4 fit to this model derived output.

Table 2 summarizes the wavenumber structure at 80 and 90 km by MCS and IUVS with comparisons to MCD for NH Case A. The amplitudes listed in Table 2 show that wavenumber-2 dominates for NH Case A in the temperature data at low altitude. While the dominant wavenumbers seen by MCS and IUVS agree, the amplitude of the wavenumbers do not. The wave amplitudes appear to be larger in the IUVS data, which may be due to the smaller number of data points in this case. The larger amplitudes could be due to the fact that small changes in amplitudes and phase are usually averaged out if more data points are included. It should be also be noted that the latitude range for the IUVS data was moved by 5°N in order to have sufficient data coverage, this change should not affect the dominant wavenumber, but may affect the amplitude of the wave. From the MCS results, the diurnal component seems to dominate the wavenumber-2 structure. For the specified Ls, MCS observations also show a consistent year-to-year picture for all Mars years with wavenumber-2 strongest and dominated by the diurnal component. MCD results reveal strong wavenumber-2 dominated by the diurnal component which is in broad agreement with MCS, although the semi-diurnal component seems to be stronger in the model. On the other hand, MCD results show equally strong wavenumber-2 and -3 when compared with IUVS. The MCD comparison was performed with MCD sampled at the same altitude, latitude, local times, longitude and Ls values as MCS and IUVS and were analyzed as explained in Sections 3.2 and 3.3.

The high altitude IUVS and NGIMS results are summarized in Table 3 with comparisons to MCD. In addition to the NGIMS derived CO_2 densities, wavenumber 1–4 fits are also performed on the Ar number densities and

Table 4
Amplitudes of the Wavenumber 1–4 Fits to the MCS and IUVS Data at 80 and 90 km Respectively Compared to MCD for NH Case B

NH Case B	IUVS T (K) @ 90 km (17–27°N)	MCD T (K) @ 90 km (17–27°N)	MCS MY 32 T (K) @ 80 km		MCS MY 28–32 T (K) @ 80 km		MCD T @ 80 km	
Mean	144 ± 2	135	146.8 ± 0.77		143.41 ± 0.59		143 ± 0.21	
			LT sum	LT diff	LT sum	LT diff	LT sum	LT diff
Wave 1	5.0 ± 1.8	**2.1**	2.1 ± 2.5	2.6 ± 1.6	1.3 ± 0.3	1.8 ± 0.2	0.8	2.08
Wave 2	**7.5 ± 2.3**	0.7	**3.3 ± 2**	**4.2 ± 1.5**	**2.7 ± 0.3**	**3.3 ± 0.6**	**4.4**	**6.39**
Wave 3	4.3 ± 2.8	1.8	0.8 ± 1.9	0.3 ± 1.2	0.6 ± 0.2	0.9 ± 0.3	1.6	2.81
Wave 4	5.1 ± 2.7	0.9	0.8 ± 1.9	1.0 ± 0.7	0.5 ± 0.2	1.5 ± 0.3	1.2	1.79

Note. The strongest wave amplitude in each column associated with data sets from each IUVS, MCS and MCD are boldfaced. Uncertainties are reported only for the observations.

Table 5
Amplitudes of the Wavenumber 1–4 Fits to the IUVS and NGIMS Data at 140 and 165 km Compared to MCD for NH Case B

NH Case B	IUVS T (K) @ 140 km	MCD IUVS T (K) @140 km	IUVS ρ (%) @ 140 km	MCD IUVS ρ (%) @ 140 km	NGIMS CO_2 ρ(%) and Ar ρ(%) @ 165 km	MCD NGIMS ρ (%) @ 165 km
Mean	189.1 ± 1.5	169	1.44e10 ± 3.25e8	6.196e9	7.91e8 ± 2.47e7	6.11e8
					2.07e7 ± 6.13e5	
Wave 1	6.8 ± 2.1	2.1	4.4 ± 3.2	5.6	3.3 ± 4.3	1.0
					3.2 ± 4.1	
Wave 2	**8.0 ± 2.1**	1.7	**17.6 ± 3.2**	8.9	**9.7 ± 4.5**	13.2
					10.2 ± 4.2	
Wave 3	**8.13 ± 2.2**	**4.3**	**17.7 ± 3.4**	**14.3**	4.7 ± 4.3	**18.1**
					4.5 ± 4.1	
Wave 4	5.7 ± 2.2	0.7	10.3 ± 3.2	1.8	4.0 ± 4.4	2.0
					5.4 ± 4.2	

Note. The strongest wave amplitude in each column associated with data sets from each IUVS, NGIMS, and MCD are boldfaced. Uncertainties are reported only for the observations.

reported in the table. The wave amplitudes derived from Ar and CO_2 can be compared with each other since both species have similar masses and scale heights and therefore provide a means to validate the results.

It is clear from Table 3 that wavenumber-2 is dominant across all IUVS and NGIMS observations in both the temperature and CO_2 densities. The wavenumbers derived from both species using NGIMS are also consistent with each other. However, comparison with MCD shows disagreement with observations at both altitudes and in both temperature and CO_2 densities. MCD results reflect the strong presence of wavenumber-3, although interestingly wavenumber-2 is second to the strongest.

For NH Case B, at lower altitude, the strongest component observed is wavenumber-2 as shown in Table 4. Both MCS and IUVS observations agree on the strongest wavenumber and from MCS, the diurnal component is shown to dominate although the semidiurnal component seems to follow closely in amplitude. The MCD comparison is consistent with this result and also sees a stronger semi-diurnal component compared to NH Case A. On comparing with IUVS, MCD shows strong wavenumber-1 which is in disagreement with the IUVS observations.

As seen in Table 5, at high altitude equally strong wavenumber-2 and wavenumber-3 are observed in both the IUVS temperatures and densities whereas NGIMS observations show a strong wavenumber-2. MCD results consistently show the presence of a strong wavenumber-3 at all high altitudes, partially agreeing with the observations. Forbes et al. (2020) report DE1 and DE2 as the dominant tides at 108 and 172 km with density perturbations that vary between 15% and 20% in the MCS latitude-Ls structure. DE2 which could be responsible for the observed wavenumber-3 structure at these thermospheric altitudes likely arises through non-linear interactions such as:

$$\mathrm{SPW1} \times \mathrm{DE1} \rightarrow D0 + \mathrm{DE2}$$

MCS results for NH Case C shown in Table 6 suggest a strong presence of both wavenumber-2 and wavenumber-4. This is in partial disagreement with the IUVS observations which suggest only the presence of a strong wavenumber-2. The year-to-year MCS observations are consistent with MCS results for this case. MCD results suggest a strong wavenumber-3 in both the MCS and IUVS comparison which is inconsistent with both observations.

Table 7 suggests strong wavenumber-2 across the high altitude IUVS and NGIMS density observations. A strong wavenumber-4 is observed in the IUVS temperatures which is consistent with the low altitude MCS temperature observations. MCD results consistently suggest strong wavenumber-2 at all high altitude which partially agrees with the observations.

Table 6
Amplitudes of the Wavenumber 1–4 Fits to the MCS and IUVS Data at 80 and 90 km Respectively Compared to MCD for NH Case C

NH Case C	IUVS T (K) @ 90 km (20°–30°N)	MCD T (K) @ 90 km (20°–30°N)	MCS MY 32 T (K) @ 80 km		MCS MY 28–32 T (K) @ 80 km		MCD T @ 80 km	
Mean	146 ± 1.6	144	141.94 ± 1.67		141.9 ± 1.13		142 ± 0.26	
			LT sum	LT diff	LT sum	LT diff	LT sum	LT diff
Wave 1	6.1 ± 1.9	0.27	2.2 ± 3.2	0.9 ± 2.5	**3.2** ± 0.4	0.9 ± 0.3	0.85	1.05
Wave 2	**8.9 ± 1.5**	3.68	**2.3 ± 4.2**	**3.6 ± 2**	1.9 ± 0.4	3.1 ± 0.4	**2.01**	3.90
Wave 3	5.9 ± 1.6	**4.30**	0.1 ± 3.3	2.9 ± 1.7	0.7 ± 0.1	2.5 ± 0.3	1.27	**6.34**
Wave 4	4.9 ± 1.6	3.68	0.9 ± 3.6	**3.6 ± 1.9**	0.4 ± 0.2	**3.7 ± 0.3**	1.14	5.34

Note. The strongest wave amplitude in each column associated with data sets from each IUVS, MCS, and MCD are boldfaced. Uncertainties are reported only for the observations.

3.8. Results for Cases South of the Equator

Of the cases selected to the south of the equator only two cases will be discussed in this section, since for the last case half of the time period is filled with the 2018 dust storm and not the entire period. Therefore our underlying assumptions for tidal analysis do not hold for this case. The cases ordered by date are October–December 2015: Case A (MY 33, Ls = 69°) and November–December 2017: Case B (MY 34, Ls = 100) which correspond to Aphelion and Winter respectively. For both cases MCS data above 82 km is unavailable and hence the wave amplitudes are sampled at 80 km in order to compare with the NH.

Tables 8 and 9 show the wave amplitudes for SH Case A at low altitude and high altitude respectively. At low altitude, the strongest component observed is wavenumber-3 across both MCS and IUVS observations. MCD results also suggest strong wavenumber-3, which is in good agreement when compared to both IUVS and MCS observations. Furthermore, the diurnal component seems to dominate the wavenumber-3 structure both in the observations as well as in MCD.

IUVS and NGIMS observations at high altitude suggest the presence of strong wavenumber-2 although IUVS temperature observations also suggest the presence of an equally strong wavenumber-3. The observed wavenumbers are also consistent across both Ar and CO_2 densities. MCD results consistently show wavenumber-2 as the strongest component which agrees partially with the IUVS and NGIMS observations. Jain et al. (2021) reported

Table 7
Amplitudes of the Wavenumber 1–4 Fits to the IUVS and NGIMS Data at 140 and 165 km Compared to MCD for NH Case C

NH Case C	IUVS T (K) @ 140 km	MCD IUVS T (K) @140 km	IUVS ρ (%) @ 140 km	MCD IUVS ρ (%) @ 140 km	NGIMS CO_2 ρ(%) and Ar ρ(%) @ 165 km	MCD NGIMS ρ (%) @ 165 km
Mean	183.1 ± 1.9	165	7.64e9 ± 1.47e8	6.37e9	4.3e8 ± 1.3e7	6.99e8
					1.2e7 ± 3.6e5	
Wave 1	3.6 ± 2.7	1.1	1.8 ± 2.7	1.1	3.6 ± 4.3	2.1
					3.9 ± 4.2	
Wave 2	6.2 ± 2.7	**2.3**	**18.8 ± 2.8**	**13.2**	**18.2 ± 4.4**	**11.3**
					17.8 ± 4.3	
Wave 3	4.0 ± 2.5	1.2	17.7 ± 2.6	9.8	16.6 ± 4.4	10.0
					14.2 ± 4.4	
Wave 4	**7.7 ± 2.8**	1.4	16.6 ± 2.8	7.0	2.3 ± 4.3	7.1
					2.6 ± 4.3	

Note. The strongest wave amplitude in each column associated with data sets from each IUVS, NGIMS and MCD are boldfaced. Uncertainties are reported only for the observations.

Table 8
Amplitudes of the Wavenumber 1–4 Fits to the MCS and IUVS Data at 80 and 90 km Respectively Compared to MCD for SH Case A

SH Case A	IUVS T (K) @ 90 km (13°–23°N) (8–11 hr)	MCD T (K) @ 90 km	MCS MY 33 T (K) @ 80 km		MCS MY 28–33 T (K) @ 80 km		MCD T @ 80 km	
Mean	138 ± 2.2	131	138.83 ± 1.05		137.33 ± 1.5		141 ± 0.19	
			LT sum	LT diff	LT sum	LT diff	LT sum	LT diff
Wave 1	5.48 ± 1.8	4.46	1.0 ± 2.3	0.9 ± 1.3	0.5 ± 0.3	1.1 ± 0.1	0.9	3.2
Wave 2	2.31 ± 2.8	2.74	0.2 ± 2.9	1.0 ± 1.3	0.3 ± 0.4	1.4 ± 0.2	1.2	0.9
Wave 3	**7.7 ± 2.6**	**5.7**	0.4 ± 2.8	**2.3 ± 1.2**	0.5 ± 0.3	**2.3 ± 0.1**	0.8	**3.9**
Wave 4	1.6 ± 2.0	1.68	**1.3 ± 2.5**	0.6 ± 1.5	**0.7 ± 0.3**	0.5 ± 0.2	**1.3**	2.9

Note. The strongest wave amplitude in each column associated with data sets from each IUVS, MCS, and MCD are boldfaced. Uncertainties are reported only for the observations.

strong wavenumber-3 amplitudes followed closely by wavenumber-2 for the same interval as discussed here for SH Case A at both 90 and 170 km. The latitude range used in the study differs from SH Case A and crosses over the equator but the local time range is similar.

For SH Case B at low altitude, the wave amplitudes shown in Table 10, suggest that wavenumber-3 is the strongest component, and agrees with the MCD results with a strong diurnal component.

At high altitude, from Table 11 it is seen that the IUVS observations suggest a strong presence of wavenumber-3 whereas NGIMS suggests a mix of wavenumbers −2 and −3. The NGIMS results for this case are also not consistent within the two species with Ar suggesting wavenumber-4 is strongest followed by wavenumber-3. It is important to note that the signals are near the noise level for the high altitude NGIMS data and hence the wavenumbers observed are weaker. Comparing with MCD, results show good agreement with the IUVS observations but only partially agree with NGIMS observations where MCD suggests the presence of strong wavenumber-2.

3.9. Overview of Spectral Components in MCD

Given that the local times in the present study are limited to fixed intervals (<4 hr LT), it is useful to examine the MCD derived temperature structures at all longitudes and local times. Spectral decomposition will provide a broad reference frame for the frequency-wavenumber content in the temperature perturbations. For the five cases

Table 9
Amplitudes of the Wavenumber 1–4 Fits to the IUVS and NGIMS Data at 140 and 165 km Compared to MCD for SH Case A

SH Case A	IUVS T (K) @ 140 km	MCD IUVS T (K) @140 km	IUVS ρ (%) @ 140 km	MCD IUVS ρ (%) @ 140 km	NGIMS CO_2 ρ(%) and Ar ρ(%) @ 165 km	MCD NGIMS ρ (%) @ 165 km
Mean	193.9±1.9	173	4.46e9±1.23e8	4.92e9	3.9e8±1.3e7	6.48e8
					1.1e7±3.4e5	
Wave 1	7.2±2.8	0.9	12.0±4.0	1.5	7.4±4.7	1.7
					6.5±4.4	
Wave 2	**11.2 ± 2.8**	**2.9**	**18.3 ± 4.1**	**13.6**	**8.3 ± 4.7**	**16.0**
					9.6 ± 4.5	
Wave 3	**10.0 ± 2.7**	1.8	14.5±3.9	11.3	3.2±4.8	10.3
					1.5±4.5	
Wave 4	4.2±2.6	0.7	10.0±3.8	2.9	4.2±4.7	3.0
					3.5±4.4	

Note. The strongest wave amplitude in each column associated with data sets from each IUVS, NGIMS, and MCD are boldfaced. Uncertainties are reported only for the observations.

Table 10
Amplitudes of the Wavenumber 1–4 Fits to the MCS and IUVS Data at 80 and 90 km Respectively Compared to MCD for SH Case B

SH Case B	IUVS T (K) @ 90 km (13–23) (8–11)	MCD T (K) @ 90 km	MCS MY 33 T (K) @ 80 km		MCS MY 28–33 T (K) @ 80 km		MCD T (K) @ 80 km	
Mean	138±2.4	131	139.80±0.8		138.4 ± 1.4		136.04±0.27	
			LT sum	LT diff	LT sum	LT diff	LT sum	LT diff
Wave 1	3.9±1.9	2.3	**1.5 ± 2.3**	0.7±1.1	**1.2 ± 0.2**	0.9±0.2	0.8	0.6
Wave 2	9.7±2.5	3.1	0.5±2.2	1.3±1.2	0.5±0.1	1.1±0.2	1.0	2.6
Wave 3	**11.9 ± 2.4**	**6.1**	0.9±2.1	**1.6 ± 0.9**	0.6±0.3	**1.8 ± 0.5**	**1.2**	**3.3**
Wave 4	5.5±2.9	2.9	1.0±2.0	0.5±1.2	0.9±0.3	0.5±0.1	0.4	2.6

Note. The strongest wave amplitude in each column associated with data sets from each IUVS, MCS, and MCD are boldfaced. Uncertainties are reported only for the observations.

examined in this study, MCD local time-longitude temperature structure are sampled and interpolated at the Ls, latitudes, and heights corresponding to each data set. In order to extract the prominent waves present in this 2D temperature field a space-time Fourier decomposition is performed by applying the FFT (fast Fourier transform) to the model derived data. Note that the wavenumbers represented in the decomposition are defined as $k = s - n$ since the temperatures are sampled in a local time reference frame.

As shown in Figure 9 the space-time Fourier decomposition of the temperature data from MCD output for NH Case A reveals that DE1 ($k = -2, n = 1 -> s = -1$) is the major contributor to the structure observed by MCS at low latitude and is followed by DE2 and S0 with nearly equal contribution. At 90 km, DE2 seems to have a slightly bigger contribution than DE1 and this corroborates the disagreement between MCD and IUVS observations as discussed in Section 3.7. DE2 seems to dominate the temperature field at 140 and 165 km followed by DE1 and SE1 but with much smaller amplitudes. The amplitudes of all the wave components are slightly larger at 165 km than at 140 km.

For NH Case B at low altitude, DE1 is the dominant component, whereas at high altitude DE2 becomes dominant followed by S0. The S0 component is second to the strongest DE1 at low altitude and almost equal in amplitude to DE2 at high altitude. A clear dominance of DE2 is seen at low altitude in NH Case C, which is followed by DE3. DE2 is still the strongest component at high altitude but with much weaker amplitude and is followed closely by DE1. Considering NH cases A and B, DE1 is likely the major contributor to the wavenumber-2 structure at

Table 11
Amplitudes of the Wavenumber 1–4 Fits to the IUVS and NGIMS Data at 140 and 165 km Compared to MCD for SH Case B

SH Case B	IUVS T (K) @ 140 km	MCD IUVS T (K) @140 km	IUVS ρ (%) @ 140 km	MCD IUVS ρ (%) @ 140 km	NGIMS CO_2 ρ(%) and Ar ρ(%) @ 165 km	MCD NGIMS ρ (%) @ 165 km
Mean	179±2.2	162	3.93e9±8.03e7	9.05e9	2.2e8±8.0e6	4.23e8
					6.5e6±2.1e5	
Wave 1	5.4±3.1	1.0	9.0±2.9	4.5	3.6±5.1	3.6
					2.9±4.7	
Wave 2	2.5±3.1	1.9	14.5±2.9	8.9	**6.1 ± 5.1**	**16.7**
					3.8±4.7	
Wave 3	**10.1 ± 3.1**	**3.8**	**18.4 ± 3.0**	**16.4**	**6.1 ± 4.9**	14.1
					4.2 ± 4.4	
Wave 4	1.8±3.0	3.2	4.6±3.0	10.0	4.1±5.0	6.1
					5.3 ± 4.6	

Note. The strongest wave amplitude in each column associated with data sets from each IUVS, NGIMS, and MCD are boldfaced. Uncertainties are reported only for the observations.

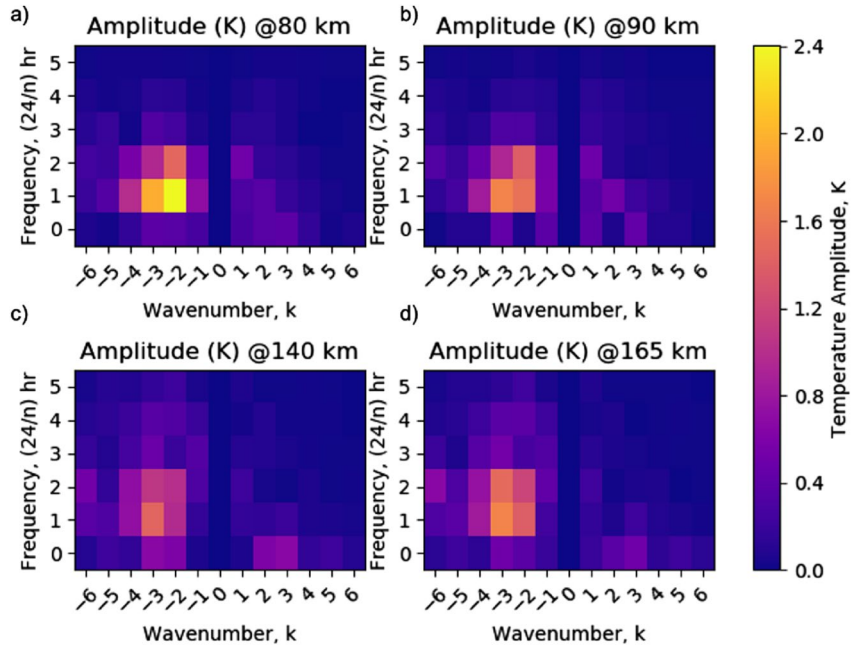

Figure 9. The Fourier decomposed temperature amplitudes as a function of frequency and wavenumber ($k = s - n$) for NH Case A, sampled at 20°N and at four altitudes 80, 90, 140, and 165 km corresponding to the each data set (MCS, IUVS at 90 and 140 km and NGIMS).

low altitude whereas the wavenumber-3 structure in NH Case C seems to be characterized by DE2 which is also the dominant component at high altitude in all three NH cases. While these results align very well with the MCD model output sampled specifically for each case, it is particularly interesting to find contributions from S0 and DE3 in addition to the strongest components.

For cases in the SH, DE2 seems to dominate the tidal field at low altitude in both cases followed by a weaker amplitude DE3, which agrees with observations suggesting the underlying component most likely responsible for the wavenumber-3 structure to be DE2. At higher altitude, in both cases, DE2 is still the strongest component but a mix of SE1 and DE1 seem to be the secondary contributors. Additionally, there is a notable difference in the amplitude of the dominant DE2 wave components between both cases wherein for Case A the amplitude seems to increase with altitude and for case B it seems to decrease with altitude. Overall, the results of the Fourier decomposition agree well with the MCD sampled data sets analyzed above and give additional insight into the tidal components possibly responsible for the observed dominant wavenumbers and confirm the discrepancies between model and observation.

4. Energy Dissipation

Vertical propagation characteristics of a wave can be inferred by examining the wave amplitude as a function of altitude assuming that the same latitudes and local times are sampled at each altitude, which is the case for the MCS data as seen in Figure 10a which shows the reconstructed wavenumber-2 amplitude as a function of altitude from the MCS LT differenced temperature data for NH Case A. Figure 10b suggests that the amplitude of the wave mostly increases with altitude roughly up to ∼80 km. For a dissipationless atmosphere, the product of atmospheric density and the square of the relative amplitude of the wave component should remain constant (Forbes, 2013; Withers et al., 2011). Hence, in the absence of dissipation, tidal amplitudes are expected to increase exponentially with altitude as density decreases to maintain constant energy density. Tidal modes that propagate vertically can be described as internal gravity waves of long periods that are influenced by the planetary rotation (Chapman & Lindzen, 1970). Such tidal modes have small positive equivalent depths and are capable of propagating energy and momentum away from their region of forcing. As such, diurnal oscillations are expected to propagate vertically equatorward and are confined within ±30° latitude, assuming background winds are small.

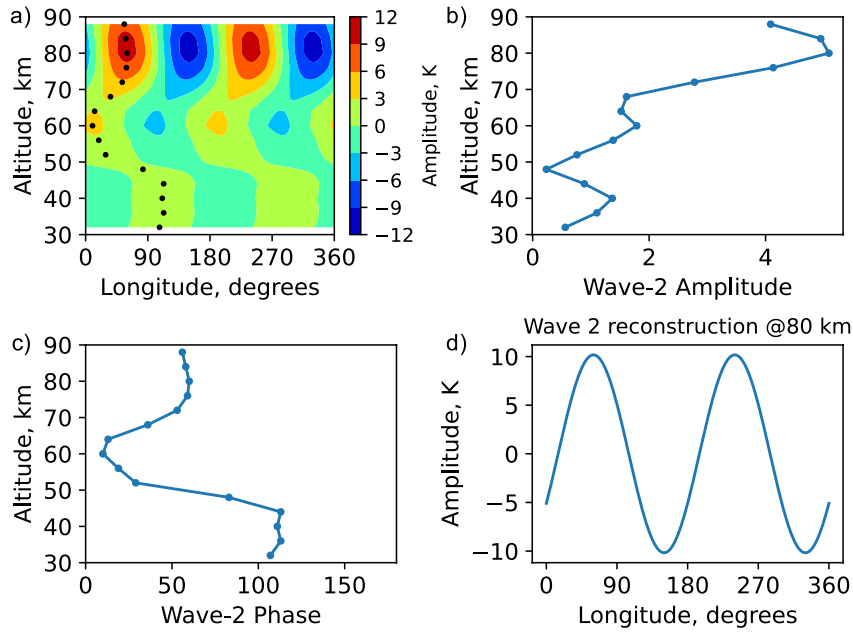

Figure 10. Panel (a) shows the wavenumber-2 reconstruction of the Mars Climate Sounder LT differenced temperature amplitudes for NH Case A, the black dots represent the phase with peak east of longitude 0°. (b) The wavenumber-2 amplitude as a function of altitude. (c) The wavenumber-2 phase as a function of altitude and (d) wavenumber-2 reconstruction at 80 km.

Within the framework of internal gravity wave theory, the Brunt-Vaisala frequency characterizes the static stability and is given by,

$$N^2(z) = \frac{g}{T_0}\left(\frac{\partial T_0}{\partial z} + \frac{g}{C_p}\right) \tag{3}$$

where g is the acceleration due to gravity on Mars, C_p is the specific heat at constant pressure and is taken as a pure CO_2 specific heat capacity (~661 J kg^{-1} K^{-1}), z is the height in km. Since the observed temperature fluctuations are associated with the vertical displacements of a fluid parcel in the atmosphere, they are also related to the available potential energy. The potential energy per unit mass E_p relative to an equilibrium position for the vertical displacement of an atmospheric fluid is given by,

$$E_p = \frac{1}{2}\left(\frac{g}{N}\right)^2\left\langle\frac{T'}{T_0}\right\rangle^2 \tag{4}$$

where N is the Brunt Vaisala frequency, T_0 is the mean temperature and T' represents the temperature perturbation about the mean temperature T_0 (Wilson et al., 1991).

Using temperature amplitudes of the dominant wavenumber in the NH (wavenumber-2) and SH (wavenumber-3) from the MCS observations, estimates of the wave potential energy are computed at three altitudes from Equation 3 and 4 which is shown as a function of altitude in Figure 10. The error bars represent the uncertainty in E_p and for the purpose of this calculation it is computed from the fractional uncertainty in the square of the relative temperature perturbation $\langle\frac{T'}{T_0}\rangle^2$ in Equation 4 alone. The uncertainty in E_p is dominated by this term and therefore the measured uncertainties are disregarded in the calculation since they are insignificant compared to the uncertainty in the fitted values. Therefore the uncertainties become nothing but twice the uncertainty in $\langle\frac{T'}{T_0}\rangle^2$. From Figures 11a and 11b it is evident that over 90% of the energy is lost between 60 and 80 km for four out of all five cases in the northern and southern hemispheres. For NH Case B about 50.4% of the energy is dissipated by 72 km followed by an increase in the energy. MCD based estimates of the normalized energy densities at the same three altitudes are also computed for the same set of conditions as the observations. The MCD estimates shown Figures 11c and 11d also show that over 90% of the energy is lost between these altitudes which is in good

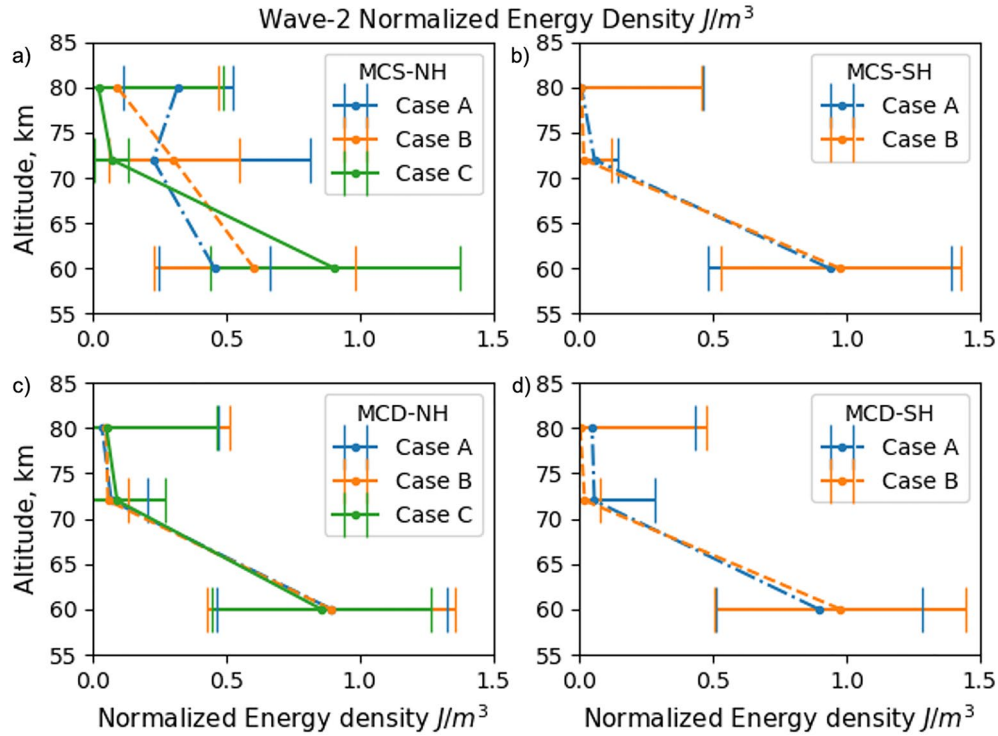

Figure 11. Normalized energy density as a function of altitude (a) and (b)—for Mars Climate Sounder observations in NH and SH respectively. Panels (c) and (d)—for Mars Climate Database derived results in the NH and SH respectively.

agreement with the observations. This lost tidal energy via dissipation most likely contributes to the heating of the atmosphere. Nakagawa et al. (2020) used IUVS stellar occultation observations to study wave perturbations in the temperature profiles due to both gravity waves and tides. This study notes wave breaking suggested by the derived negative buoyancy frequencies in the 70–100 km altitude regime which is similar to the MCS sampled altitudes where tidal dissipation is being observed.

5. Summary and Conclusions

This study uses a combination of observations from the IUVS, NGIMS and MCS instruments to examine atmospheric tides in the Martian atmosphere observed at different altitudes concurrently. By choosing a narrow latitude and local time range, six cases at low latitudes are identified, three in each of the northern and southern hemispheres. Of the three southern hemisphere cases data from only two are used in this study. The cases belonging to different Ls, enable the comparison of interannual and seasonal change. Given a specified Ls, as indicated by the analysis here, MCS mean temperatures show a consistent year-to-year picture with almost constant mean temperature for all MYs (28–34) in both the NH and SH.

Dealing first with the NH results in the 80–90 km altitude region, we find the following:

- The MCS mean temperatures at 88 km are in good agreement with the IUVS mean temperatures at 90 km in the NH. A strong wavenumber-2 structure is revealed in the derived temperatures from both MCS sampled at 80 km and IUVS at 90 km. MCS observations reveal that the diurnal component is strongest with semidiurnal mixed in some cases, which is also captured well by the MCD model output although the amplitude of the semidiurnal component is slightly overestimated by the model.

  On comparing the IUVS observations at 90 km with MCD model output we see that they do not agree well in dominant wavenumber. The IUVS observations suggest a strong wavenumber-2 in all cases but the model results suggest wavenumber-3 to be dominant in Case A and Case C. This disagreement between IUVS observations and the model is in contrast with the MCS observations at 80 km, where there is a reasonably good agreement with the model.

- The MCS averaged wave amplitudes at 80 km from MY 28–32 for the same Ls defined for each case - A, B, and C are shown in Tables 2, 4, and 6 and indicate that there is very little interannual variability in the dominant wavenumber from one Mars year to another. Therefore, at least at these altitudes, for a specified Ls we could predict next year based on the past several years as demonstrated in this analysis. It also worth noting that the diurnal component remains dominant year after year as well.
- On the other hand, seasonal variation in the NH can be seen in the MCS derived wave amplitudes, where the wavenumber-2 signature is strongest in two out of three cases in the NH, both during Northern winter. But for NH Case C during Aphelion (MY34, Ls = 71°), the strongest signature seen is wavenumber-4 followed closely by wavenumber-2. The primary contribution to the wavenumber-4 in the LT differenced temperatures is expected to be from DE3. Guzewich et al. (2012) reported the first detection of DE3 in the MCS temperature data but for a different season than Aphelion from Ls 135–225° which is northern fall equinox.
- Further, energy derived for the diurnal component of the dominant wavenumber from the MCS observations reveals that most of the energy in the tide is dissipated between 60 and 80 km. This energy is deposited into the mean atmosphere and presumably contributes to its heating and acceleration.

Dealing next with the NH results in the 140–165 km altitude region, we find the following:

- At high altitude in the NH, the CO_2 densities and temperatures from the IUVS, and the CO_2 densities from NGIMS reveal a strong wavenumber-2 signature mixed with some wavenumber-3. For NH Case B, the wavenumber-3 signature is equally strong and a mechanism that could give rise to such change in wavenumber at high altitude is non-linear wave-wave interaction with the stationary planetary wave. In general, the same tidal signature is captured in both the IUVS temperatures and densities, except in NH Case C where a slightly stronger wavenumber-4 is seen in the IUVS temperatures. The variation in the temperature data is in near perfect anti-phase with the density variation which is consistent with England et al. (2019).
- NGIMS observations agree in dominant wavenumber with the IUVS in all three cases, and have similar phases in both data sets.
- All wavenumbers derived using NGIMS Ar and CO_2 are consistent with each other.
- Comparing the high altitude results in the NH to MCD model output reveals that the model does not capture the dominant wavenumber seen in the observations.

Dealing with the SH results in the 80–90 km altitude region, we find the following:

- In the SH, at lower altitude both the MCS and IUVS derived temperatures reveal a strong wavenumber-3 signature. The dominant wavenumber-3 seen in both the IUVS observations at 90 km and the MCS observations at 80 km are captured well by the MCD model output with comparable amplitudes. This is in contrast with the dominant wavenumber-2 observed in the NH cases and is expected. Forbes et al. (2020) found that the eastward propagating DE1, DE2 and DE3 tides had the largest contribution by examining MCD height-latitude structures. The authors also note the contribution of symmetric and anti-symmetric modes of each component leading to a shift in the latitudinal maxima with height which could explain the hemispheric differences seen in the observed dominant wavenumber. Furthermore, vertical propagation of these components are favored by the mean zonal winds thereby enabling the generation of large perturbations at thermospheric altitudes.
- MCS observations in the SH also reveal a strong diurnal component with semidiurnal mixed in some cases, which is again captured very well by the MCD model output with comparable amplitudes.
- Similar to the NH, very little interannual variability is seen in the dominant wavenumber from one Mars year to another given an Ls which again allows to predict the next year.
- Seasonal change like the NH is not observed in the MCS data, given that the same dominant wavenumber is seen in both cases of which one is during winter and the other aphelion.
- Again, just like the NH most of the energy is dissipated within this altitude range between 60 and 80 km in the SH as well.

Dealing next with the SH results in the 140–165 km altitude region, we find the following:

- At higher altitude in the SH, the CO_2 densities and temperatures from the IUVS and CO_2 densities from the NGIMS suggests a mix of wavenumber-2 and -3 with both wavenumbers being dominant about 50% of the

time. MCD model estimates of the wave amplitudes agree with the observations over half the time which is better than the NH.

- Wavenumbers derived using NGIMS Ar and CO_2 are consistent for SH Case A where the same dominant wavenumber-2 is observed in both species, whereas for SH Case B the CO_2 density perturbations reveal a mix of equally strong wavenumber-2 and wavenumber-3, whereas Ar suggests a mix wavenumber-4 followed closely by wavenumber-3. But note that all three observed wavenumbers in this case (Case B) are consistent within their error bars.
- In summary, at least at low altitudes for two out of three NH cases, the primary contribution to the wavenumber-2 structure is likely from the DE1 component. This diurnal component is also captured well by the model at these altitudes. However, at high altitudes, the model does not agree very well with the observed wavenumber-2 structure seen in these cases, and instead, a mix of wavenumber-3 and -2 is seen. The Fourier decomposition of the MCD output suggests the biggest contributions at these higher altitudes are from DE2 and DE1. Generally, MCD model outputs capture the dominant wavenumbers better at lower altitude than at high altitude. The interannual variations at the low altitudes are very small in both NH and SH cases whereas seasonal variations are present in the NH but not in the SH. But at high altitudes, these variations are more evident as other wavenumbers start becoming dominant. From the observations used in this study, it is not possible to fully determine why the agreement of the MCD model output is lacking at the higher altitudes than lower, but possibilities include: differences in the simulated and actual upward propagation of one or more of the dominant tides; in situ generation of one of the waves observed that is not captured in the model or vice versa; changes in the latitudinal structure of the tides that differs between the model and the atmosphere; differences in modeled mean wind and temperatures than those at Mars. Additional data sets, including those that extend this to other latitudes could likely help resolve this.

To summarize, measurements from the IUVS and NGIMS instruments on board the MAVEN spacecraft are used in conjunction with measurements from the MCS instrument aboard MRO to investigate the presence of tides and variations in their amplitudes seasonally and interannually. Observations are also compared with MCD derived output for the same intervals considered therein. The estimates of energy derived in this study suggest that very little of the total energy that the tides begin with is getting into the Martian thermosphere. However, this is in contrast to the very large amplitude wave structure observed in the thermosphere which is due to the very small mean density seen at this altitude. While these waves are very significant to the Martian thermosphere, much of the wave energy is lost before it reaches this region. Slipski et al. (2018) showed that below 80 km, dissipation occurs due to reduced stability whereas in the lower thermosphere waves propagate with height if there is high static stability and low molecular viscosity in the atmosphere. The findings from this study suggest that waves are expected to dissipate between 20 and 70 km, whereas the stability in the thermosphere below 160 km encourages free wave propagation which complements the results obtained in the analysis reported here. Exploring the impacts of dissipation in this region could allow future studies to elucidate its effects in the context of dynamics, mixing, and so on.

Data Availability Statement

The IUVS periapse level 1C (version 13 revision 1), IUVS periapse level 2 data (version 13 revision 1), NGIMS level 2 data (version 8 revision 1) and the MCS data used in this analysis are archived in NASA's Planetary Data System (PDS) at https://atmos.nmsu.edu/data_and_services/atmospheres_data/MAVEN/maven_iuvs.html (Deighan, 2015), https://pds-atmospheres.nmsu.edu/data_and_services/atmospheres_data/MAVEN/ngims.html (Benna & Lyness, 2014) and https://atmos.nmsu.edu/data_and_services/atmospheres_data/MARS/atmosphere_temp_prof.html respectively. The MAVEN mission has been funded by NASA through the Mars Exploration Program. The Mars Climate Database (MCD) model output used in this study are available by requesting the full version of MCD v5.3 on http://www-mars.lmd.jussieu.fr/mars/MCD_pro/mcd_pro.html (Forget et al., 1999; Millour et al., 2017). The data products associated with this manuscript are derived from the data sets cited above and are archived in the FAIR-compliant VT library permanent repository available at https://doi.org/10.7294/19755502 (Kumar, 2022).

Acknowledgments
This work was supported through NASA Grant No. 80NSSC20K1050.

References

Benna, M., & Lyness, E. (2014). MAVEN neutral gas and ion mass spectrometer data. https://doi.org/10.17189/1518931

Bougher, S. W., Engel, S., Hinson, D. P., & Forbes, J. M. (2001). Mars Global Surveyor radio science electron density profiles: Neutral atmosphere implications. *Geophysical Research Letters*, *28*(16), 3091–3094. https://doi.org/10.1029/2001GL012884

Chapman, S., & Lindzen, R. S. (1970). *Atmospheric tides: Thermal and gravitational* (p. 200). Gordon and Breach.

Deighan, J. (2015). Mars Atmosphere and Volatile Evolution (MAVEN) imaging ultraviolet spectrograph (IUVS) derived-level data product bundle. https://doi.org/10.17189/1518956

England, S. L., Liu, G., Kumar, A., Mahaffy, P. R., Elrod, M., Benna, M., et al. (2019). Atmospheric tides at high latitudes in the Martian upper atmosphere observed by MAVEN and MRO. *Journal of Geophysical Research: Space Physics*, *124*(4), 2943–2953. https://doi.org/10.1029/2019JA026601

England, S. L., Liu, G., Withers, P., Yiğit, E., Lo, D., Jain, S., et al. (2016). Simultaneous observations of atmospheric tides from combined in situ and remote observations at Mars from the MAVEN spacecraft: In situ and remote observations of tides. *Journal of Geophysical Research: Planets*, *121*(4), 594–607. https://doi.org/10.1002/2016JE004997

Evans, J. S., Stevens, M. H., Lumpe, J. D., Schneider, N. M., Stewart, A. I. F., Deighan, J., et al. (2015). Retrieval of CO_2 and N_2 in the Martian thermosphere using dayglow observations by IUVS on MAVEN. *Geophysical Research Letters*, *42*(21), 9040–9049. https://doi.org/10.1002/2015GL065489

Fang, X., Forbes, J. M., Gan, Q., Liu, G., Thaller, S., Bougher, S., et al. (2021). Tidal effects on the longitudinal structures of the Martian thermosphere and topside ionosphere observed by MAVEN. *Journal of Geophysical Research: Space Physics*, *126*(2), e2020JA028562. https://doi.org/10.1029/2020JA028562

Forbes, J. M. (2013). Tidal and planetary waves. In R. M. Johnson & T. L. Killeen (Eds.), *Geophysical Monograph Series* (pp. 67–87). American Geophysical Union. https://doi.org/10.1029/GM087p0067

Forbes, J. M., Bridger, A. F. C., Bougher, S. W., Hagan, M. E., Hollingsworth, J. L., Keating, G. M., & Murphy, J. (2002). Nonmigrating tides in the thermosphere of Mars. *Journal of Geophysical Research*, *107*(E11), 23-1–23-12. https://doi.org/10.1029/2001JE001582

Forbes, J. M., & Hagan, M. E. (2000). Diurnal Kelvin wave in the atmosphere of Mars: Towards an understanding of 'stationary' density structures observed by the MGS accelerometer. *Geophysical Research Letters*, *27*(21), 3563–3566. https://doi.org/10.1029/2000GL011850

Forbes, J. M., Zhang, X., Forget, F., Millour, E., & Kleinböhl, A. (2020). Solar tides in the middle and upper atmosphere of Mars. *Journal of Geophysical Research: Space Physics*, *125*(9), e2020JA028140. https://doi.org/10.1029/2020JA028140

Forget, F., Hourdin, F., Fournier, R., Hourdin, C., Talagrand, O., Collins, M., et al. (1999). Improved general circulation models of the Martian atmosphere from the surface to above 80 km. *Journal of Geophysical Research*, *104*(E10), 24155–24175. https://doi.org/10.1029/1999JE001025

González-Galindo, F., López-Valverde, M. A., Forget, F., García-Comas, M., Millour, E., & Montabone, L. (2015). Variability of the Martian thermosphere during eight Martian years as simulated by a ground-to-exosphere global circulation model. *Journal of Geophysical Research: Planets*, *120*(11), 2020–2035. https://doi.org/10.1002/2015JE004925

Guzewich, S. D., Talaat, E. R., & Waugh, D. W. (2012). Observations of planetary waves and nonmigrating tides by the Mars Climate Sounder. *Journal of Geophysical Research*, *117*(E3), E03010. https://doi.org/10.1029/2011JE003924

Jain, S. K., Soto, E., Evans, J. S., Deighan, J., Schneider, N. M., & Bougher, S. W. (2021). Thermal structure of Mars' middle and upper atmospheres: Understanding the impacts of dynamics and solar forcing. *Icarus*, 114703. https://doi.org/10.1016/j.icarus.2021.114703

Keating, G. M., Bougher, S. W., Zurek, R. W., Tolson, R. H., Cancro, G. J., Noll, S. N., et al. (1998). The structure of the upper atmosphere of Mars: In situ accelerometer measurements from Mars Global Surveyor. *Science*, *279*(5357), 1672–1676. https://doi.org/10.1126/science.279.5357.1672

Kumar, A. (2022). Data associated with "Observations of atmospheric tides in the middle and upper atmosphere of Mars from MAVEN and MRO" [Dataset]. University Libraries, Virginia Tech. https://doi.org/10.7294/19755502

Lee, C., Lawson, W. G., Richardson, M. I., Heavens, N. G., Kleinböhl, A., Banfield, D., et al. (2009). Thermal tides in the Martian middle atmosphere as seen by the Mars Climate Sounder. *Journal of Geophysical Research*, *114*(E3), E03005. https://doi.org/10.1029/2008JE003285

Liu, G., England, S., Lillis, R. J., Mahaffy, P. R., Elrod, M., Benna, M., & Jakosky, B. (2017). Longitudinal structures in Mars' upper atmosphere as observed by MAVEN/NGIMS. *Journal of Geophysical Research: Space Physics*, *122*(1), 1258–1268. https://doi.org/10.1002/2016JA023455

Lo, D. Y., Yelle, R. V., Schneider, N. M., Jain, S. K., Stewart, A. I. F., England, S. L., et al. (2015). Nonmigrating tides in the Martian atmosphere as observed by MAVEN IUVS. *Geophysical Research Letters*, *42*(21), 9057–9063. https://doi.org/10.1002/2015GL066268

Mahaffy, P. R., Benna, M., King, T., Harpold, D. N., Arvey, R., Barciniak, M., et al. (2015). The neutral gas and ion mass spectrometer on the Mars atmosphere and volatile evolution mission. *Space Science Reviews*, *195*(1–4), 49–73. https://doi.org/10.1007/s11214-014-0091-1

Mazarico, E., Zuber, M. T., Lemoine, F. G., & Smith, D. E. (2008). Observation of atmospheric tides in the Martian exosphere using Mars Reconnaissance Orbiter radio tracking data. *Geophysical Research Letters*, *35*(9), L09202. https://doi.org/10.1029/2008GL033388

McCleese, D. J., Schofield, J. T., Taylor, F. W., Calcutt, S. B., Foote, M. C., Kass, D. M., et al. (2007). Mars Climate Sounder: An investigation of thermal and water vapor structure, dust and condensate distributions in the atmosphere, and energy balance of the polar regions. *Journal of Geophysical Research*, *112*(E5), E05S06. https://doi.org/10.1029/2006JE002790

McClintock, W. E., Schneider, N. M., Holsclaw, G. M., Clarke, J. T., Hoskins, A. C., Stewart, I., et al. (2015). The Imaging Ultraviolet Spectrograph (IUVS) for the MAVEN Mission. *Space Science Reviews*, *195*(1–4), 75–124. https://doi.org/10.1007/s11214-014-0098-7

Millour, E., Forget, F., Spiga, A., Vals, M., Zakharov, V., Navarro, T., et al. (2017). The Mars Climate Database (MCD version 5.3) In *Presented at the EGU General Assembly Conference Abstracts* (p. 12247).

Nakagawa, H., Terada, N., Jain, S. K., Schneider, N. M., Montmessin, F., Yelle, R. V., et al. (2020). Vertical propagation of wave perturbations in the middle atmosphere on Mars by MAVEN/IUVS. *Journal of Geophysical Research: Planets*, *125*(9), e2020JE006481. https://doi.org/10.1029/2020JE006481

Schneider, N. M., Milby, Z., Jain, S. K., González-Galindo, F., Royer, E., Gérard, J.-C., et al. (2020). Imaging of Martian circulation patterns and atmospheric tides through MAVEN/IUVS nightglow observations. *Journal of Geophysical Research: Space Physics*, *125*(8), e2019JA027318. https://doi.org/10.1029/2019JA027318

Slipski, M., Jakosky, B. M., Benna, M., Elrod, M., Mahaffy, P., Kass, D., et al. (2018). Variability of Martian turbopause altitudes. *Journal of Geophysical Research: Planets*, *123*(11), 2939–2957. https://doi.org/10.1029/2018JE005704

Thaller, S. A., Andersson, L., Pilinski, M. D., Thiemann, E., Withers, P., Elrod, M., et al. (2020). Tidal wave-driven variability in the Mars ionosphere-thermosphere system. *Atmosphere*, *11*(5), 521. https://doi.org/10.3390/atmos11050521

Wilson, R., Chanin, M. L., & Hauchecorne, A. (1991). Gravity waves in the middle atmosphere observed by Rayleigh lidar: 2. Climatology. *Journal of Geophysical Research*, *96*(D3), 5169. https://doi.org/10.1029/90JD02610

Withers, P., Bougher, S. W., & Keating, G. M. (2003). The effects of topographically-controlled thermal tides in the Martian upper atmosphere as seen by the MGS accelerometer. *Icarus*, *164*(1), 14–32. https://doi.org/10.1016/S0019-1035(03)00135-0

Withers, P., Pratt, R., Bertaux, J.-L., & Montmessin, F. (2011). Observations of thermal tides in the middle atmosphere of Mars by the SPICAM instrument. *Journal of Geophysical Research*, *116*(E11), E11005. https://doi.org/10.1029/2011JE003847

Zurek, R. W. (1976). Diurnal tide in the Martian atmosphere. *Journal of the Atmospheric Sciences*, *33*(2), 321–337. https://doi.org/10.1175/1520-0469